



## **The influence of geometrical and material imperfections on the stability and resistance of I and H sections**

Lucile Gérard<sup>1</sup>, Caroline Arsenault<sup>2</sup>, Markus Kettler<sup>3</sup>, Nicolas Boissonnade<sup>4</sup>

### **Abstract**

The design of steel structures has been deeply studied and reliable guidelines are provided in current standards. The ultimate resistance of open-sections such as I and H shapes depends on their buckling behaviour which is highly sensitive to the level of imperfections enhanced on the section. Extensive studies and experimental measurements on imperfections have been realised over the years, which enabled the improvement of standards recommendations.

However, with the emergence and improvement of Finite Element software, these standards exhibit lack of information for the introduction of geometrical and structural imperfections into FE models. Therefore, numerical simulations were performed with the purpose of providing reliable and efficient recommendations.

The current paper presents investigations related to the influence of geometrical and material imperfections on the local resistance of I and H sections. A consistent and convenient approach for their introduction into a Finite Element model is provided afterwards.

### **1 Introduction**

Nowadays, steel is considered as one of the major materials used in construction. Among the panel of sections available within the industry, hot-rolled and welded I and H sections are useful both in the field of bridge construction and within building applications. Designing steel structures represents a main challenge since steel structures undergo peculiar behaviour under compressive forces. Indeed, under compression, elements made of sections such as I and H shapes are prone to suffer from local buckling as well as from global buckling (e.g flexural buckling and lateral torsional buckling). Furthermore, both the ultimate resistance and the stability of an open-section are highly influenced by the level of imperfections affecting the section. As a matter of fact, throughout the manufacturing process, the shaping of the sections generates imperfections such as residual stresses, eccentricities and out of straightness among other defaults. These imperfections reduce the cross-section strength and can induce premature yielding, earlier buckling and, consequently, failure. For many years, research investigations involving measurements of imperfections taking part of experimental campaigns were realised.

---

<sup>1</sup> Graduate Student, Laval University, < lucile.gerard.1@ulaval.ca >

<sup>2</sup> Graduate Student, Laval University, < caroline.arsenault.10@ulaval.ca >

<sup>3</sup> Assistant Professor, Graz University of Technology, < Kettler@tugraz.at >

<sup>4</sup> Professor, Laval University, < nicolas.boissonnade@gci.ulaval.ca >

However, even though a great quantity of information is available with respect to the reality of imperfections, with the emergence and amelioration of Finite Element software; the introduction of imperfections into the numerical simulations represents a strategic challenge.

Many standard guidelines and recent methods dedicated to steel design are available. However, the design recommendations suggested in codes and dedicated to the use of non-linear analyses by means of Finite Element simulations exhibit discrepancies, lack of usability and inaccuracies especially according to the introduction of imperfections. Thus, when non-linear analyses are required, the use of FE software is frequently avoided even though it would provide an excellent and reliable ultimate load-carrying capacity if wisely used.

The current paper presents herein a study carried out on the influence of imperfections on the cross-sectional ultimate load-carrying capacity of open-sections and, thereafter, provides recommendations for the introduction of imperfections into numerical simulations.

Respecting to local geometrical imperfections, the Eurocode (Eurocode 2007) suggests using the 1<sup>st</sup> eigenmode shape with an amplification factor corresponding to the minimum value between  $\frac{a}{200}$  and  $\frac{b}{200}$ , using 80% of geometrical tolerances, where  $a$  and  $b$  refer to the height and width of the plate. Then, if residual stresses are added to the FE model, the Eurocode guidelines indicate the possibility to apply a reduction of 30% to the secondary imperfection if a leading imperfection is selected. However, the standard does not provide any guidance with respect to the adoption of a suitable residual stress pattern. In most cases, these brief recommendations lead to over-conservative results and loss of resistance.

Kettler has been investigating the plastic capacity of semi-compact sections, and, in doing so, carried out an experimental campaign on hot-rolled and welded H-sections (Kettler 2008). To compare the specimen resistance obtained from the tests with results provided by numerical simulations, a FE model was developed where both geometrical and material initial imperfections were based on experimental measurements. Yun realised a similar work for the introduction of geometrical imperfections into a FE model following experimental tests on hot-rolled H-profiles (Yun, et al. 2016). Davids and Hancock introduced geometrical imperfections from test measurements through a cubic polynomial curve fitting program (Davids et Hancock 1986).

Furthermore, many researchers such as Kettler (Kettler 2008), employed the first buckling mode shape obtained from linear buckling analysis and magnified with a suitable amplification factor. Otherwise, other procedures were employed for the introduction of imperfections e.g the modification of nodes coordinates by means of sinusoidal functions (Boissonnade et Somja 2012).

In addition to initial geometrical imperfections, a profile bears material imperfections as residual stress states. After manufacturing, the residual stress state is auto-equilibrated on the section i.e it will not induce additional forces before loading. For sections whose failure is caused by a combination of yielding and buckling, residual stresses induce premature yielding of some fibres of the section, and, consequently, cause stiffness reductions which can lead to the earlier occurrence of buckling.

Within literature, various patterns have been considered, whether they relied on plate-per-plate equilibrated schemes or distributions equilibrated within the whole cross-section. Respecting to hot-rolled profiles, membrane residual stresses are induced by the uneven cooling of steel after being manufactured. Welding induces uneven cooling as well. The yield limit can be reached on the tension areas near welds where the material has been highly heated or where the plates have been obtained by flame cutting. The amplitudes and distributions depends on various aspects such as the cross-section geometry or the procedures and temperature employed

within fabrication. This kind of information is usually delicate to obtain. Data provided by some manufacturers has been studied and conclusions made on these results and encountered in papers are deeply explored. Moreover, several researchers have been measuring residual stresses on specimens throughout extensive experimental campaigns (Kettler 2008), (Thiébaud, et al. 2016), (Davids et Hancock 1986). However, the measurement of residual stresses exhibit several sources of difficulties and their reliability remains questionable (James 2010).

Even though, the FE modelling of geometrical and material imperfections has been deeply studied for many years, it still requires further investigation to provide reliable guidance.

The study presented herein will focus on the influence of geometrical and material imperfections on the local resistance with the objective to provide guidelines for the introduction of imperfections into FE simulations.

First of all, the Finite Element model features and assumptions are described in section 2. This section also contains a brief presentation of the geometrical and material imperfections considered for the study. Thereafter, investigations towards the influence of geometrical imperfections on the local load-bearing capacity of open-sections is presented in section 3. Then, results and observations related to the influence of material imperfections are shown in section 4. To conclude, section 5 provides recommendations for the introduction of geometrical and material imperfections into FE simulation.

## **2 Development of Finite Element models**

### *2.1 Basic features and assumptions*

Numerical simulations were performed by means of the Finite Element software FINELg, developed in collaboration between ULg (University of Liège) and Greish structural office (Belgium). Analyses such as linear buckling analyses (LBA), materially non-linear analyses (MNA) and fully non-linear analyses with imperfections (GMNIA) were carried out based on a verified Finite Element model. To this end, experimental data were gathered and compared with numerical results to validate the FE model considered thereafter.

As a matter of fact, previously to the current investigation, the Finite Element model was compared to experimental results obtained during a test campaign carried out on hot-rolled and welded H-profiles and realised by Kettler (Kettler 2008) at Graz University. To do so, numerical simulation input parameters were carefully chosen to fit with the test setup used back then. Consequently, a valuable agreement between experimental and numerical results was achieved, which assessed the reliability of the model.

The elements employed throughout the study were quadrangular shell elements (QSCRA) based on Kirchoff's theory regarding bending in addition to membrane theory for in-plane stresses. Total corotational Lagrangian formulation taking due account of the current deflected state of the element and with reduced integration were used with 7 integration points through the thickness using Gauss numerical integration method. A reliable and time-efficient model mesh was adopted following extensive mesh density studies on both hot-rolled and welded Finite Element models. The same sections as those considered within this paper were studied.

Specific precautions were employed in the modelling of the web-to-flange junction (see Figure 1) of hot-rolled sections. To create an accurate and advanced model, the fillet zones were replaced by a beam element located at the centre of gravity of the two corner zones (Greiner, et al. 2007). Moreover, due to the disposition of nodes, an overlap between elements occurred at the web/flange intersection. Hence, the beam element area selected corresponds to the two corners area from which the overlap was removed (Boissonnade et Somja 2012).

In addition, since the web-to flange junction of the section enhances important rigidity which prevent this area to suffer of local buckling, an additional truss element was introduced into the Finite Element model to respect the effective plate length prone to suffer from local instability.

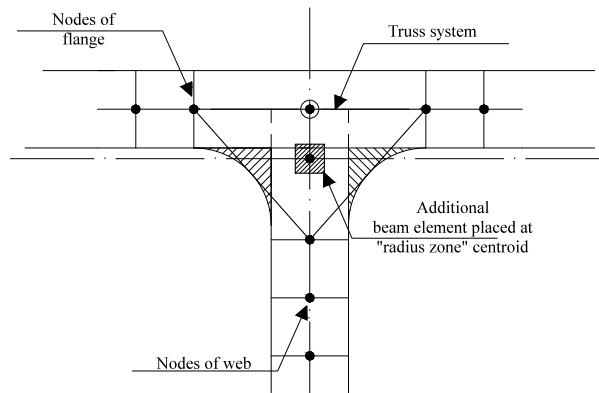


Figure 1: Web-to-flange junction modelling of a hot-rolled section.

As for welded sections, since the welds do not provide a significant restraint to avoid the web and flanges to suffer from local buckling, no such truss elements were introduced at the web-to-flange junction.

The stress-strain constitutive law employed and represented on Figure 2 includes a plastic plateau followed by suitable strain-hardening part. The strengthening slope value and the strain boundaries result from previous studies (Hayeck 2016). The material law enhanced thereafter is suitable for standard yield limit such as  $f_y = 235 \text{ MPa}$  and  $f_y = 460 \text{ MPa}$  which were considered in the current study.

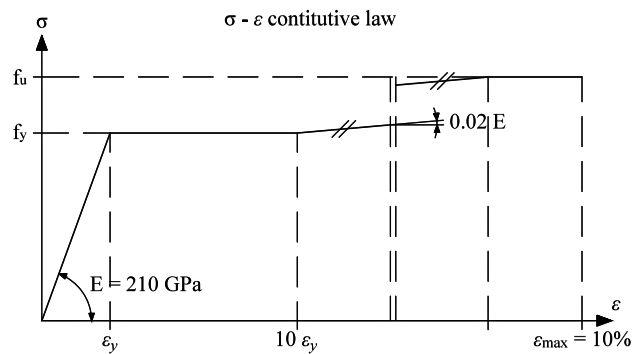


Figure 2: Material properties considered in the Finite Element model.

With respect to support conditions, fork conditions were applied at both ends and axial displacement was constrained at one end. Moreover, linear constraints were defined for the deformed section to stay conform to the beam theory assumptions. Thus, the deformation of the “x-constrained nodes” is fixed as a combination of the 4 loading cases: axial compression, major axis bending, minor axis bending and warping. The 4 “x-free nodes” located at the 4 extremities govern the deformation of all the other nodes of the section.

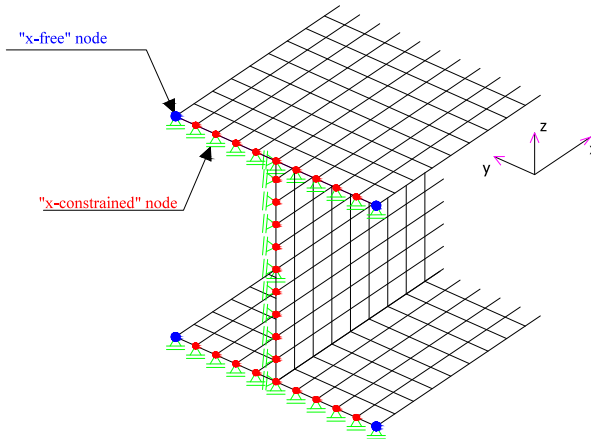


Figure 3: Constraints imposed to the FE model.

The loading is applied at the 4 extreme nodes of the cross-section by means of suitable definitions of axial forces, for all load cases. For the standard parametric studies, sections under pure compression and pure major axis bending were studied. Furthermore, with respect to the peculiar sub-study dedicated to compare numerical results to experimental test results, simple and combined load cases were investigated.

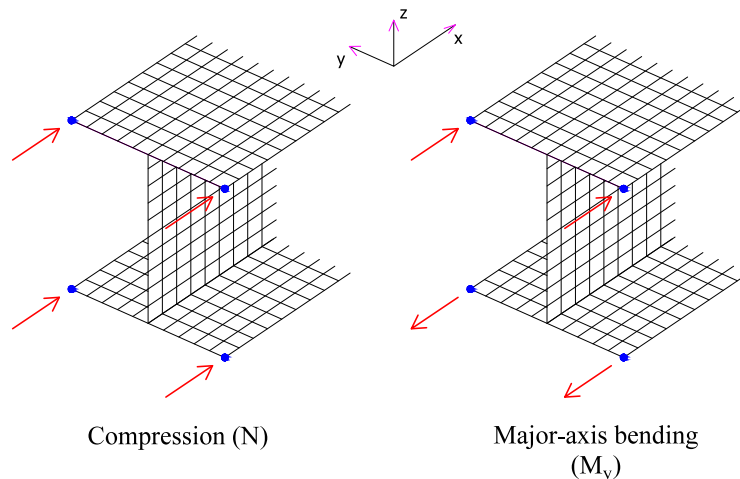


Figure 4: Loading situations applied to the FE model.

A large range of geometries were studied, covering compact to very slender sections for both I and H shapes sections. In order to include more slender sections, two geometries were invented: IPES and HEAS. The following sections were considered under pure compression and pure major-axis bending:

- IPE 140 ( $h=140\text{mm}$ ;  $b=73\text{mm}$ ;  $t_w=4,7\text{mm}$ ;  $t_f=6,9\text{mm}$ ;  $r=7\text{mm}$ ;  $b/h=0,52$ )
- IPE 400 ( $h=400\text{mm}$ ;  $b=180\text{mm}$ ;  $t_w=8,6\text{mm}$ ;  $t_f=13,5\text{mm}$ ;  $r=21\text{mm}$ ;  $b/h=0,45$ )
- IPES ( $h=800\text{mm}$ ;  $b=220\text{mm}$ ;  $t_w=10\text{mm}$ ;  $t_f=19\text{mm}$ ;  $r=24\text{mm}$ ;  $b/h=0,28$ )
- HEA160 ( $h=152\text{mm}$ ;  $b=160\text{mm}$ ;  $t_w=6\text{mm}$ ;  $t_f=9\text{mm}$ ;  $r=15\text{mm}$ ;  $b/h=1,05$ )
- HEA 600 ( $h=590\text{mm}$ ;  $b=300\text{mm}$ ;  $t_w=13\text{mm}$ ;  $t_f=25\text{mm}$ ;  $r=27\text{mm}$ ;  $b/h=0,51$ )
- HEAS ( $h=300\text{mm}$ ;  $b=300\text{mm}$ ;  $t_w=6\text{mm}$ ;  $t_f=10\text{mm}$ ;  $r=27\text{mm}$ ;  $b/h=1$ )

With respect to the length of the member, the size was chosen sufficiently short to avoid the occurrence of global buckling and long enough to reduce the influence of support conditions. Moreover, the member length chosen depends on the local geometrical imperfection pattern to ensure the number of half-waves and sinusoidal period desired (see Table 1).

However, for the comparison between numerical simulations and experimental results gathered from a campaign realised at Graz University (Kettler 2008), the same load cases and cross-section geometries were investigated throughout various numerical simulations (see section 3.1).

## 2.2 Material imperfections

Material imperfections are consecutive to the manufacturing process. Since their production process differs, hot-rolled and welded sections exhibit different types of residual stresses whether in their amplitude or in their distribution. The patterns chosen as part of this study are plate per plate equilibrated which enables the presence of a residual compressive stress at the 1<sup>st</sup> step of load application without generation of additional eccentric force.

Two different amplitudes and two various pattern shapes dedicated to hot-rolled sections were considered (see Figure 5 a) and b)) based on previous European recommendations (ECCS - Committee 8 - Stability 1976 1976). As for welded sections, two different residual stress pattern were introduced which differ both in their amplitude and shape (see Figure 5 c) and d)). These patterns consist in a rectangular pattern, recommended by the Eurocode (ECCS - Committee 8 - Stability 1976 1976) and a trapezoidal pattern provided by Kettler through the Semi-Comp project (Greiner, et al. 2007) based on experimental measurements. Constants  $\alpha_1$  and  $\alpha_2$  can be calculated from the section geometrical properties under the assumption of plate-per-plate equilibrated residual stress patterns.

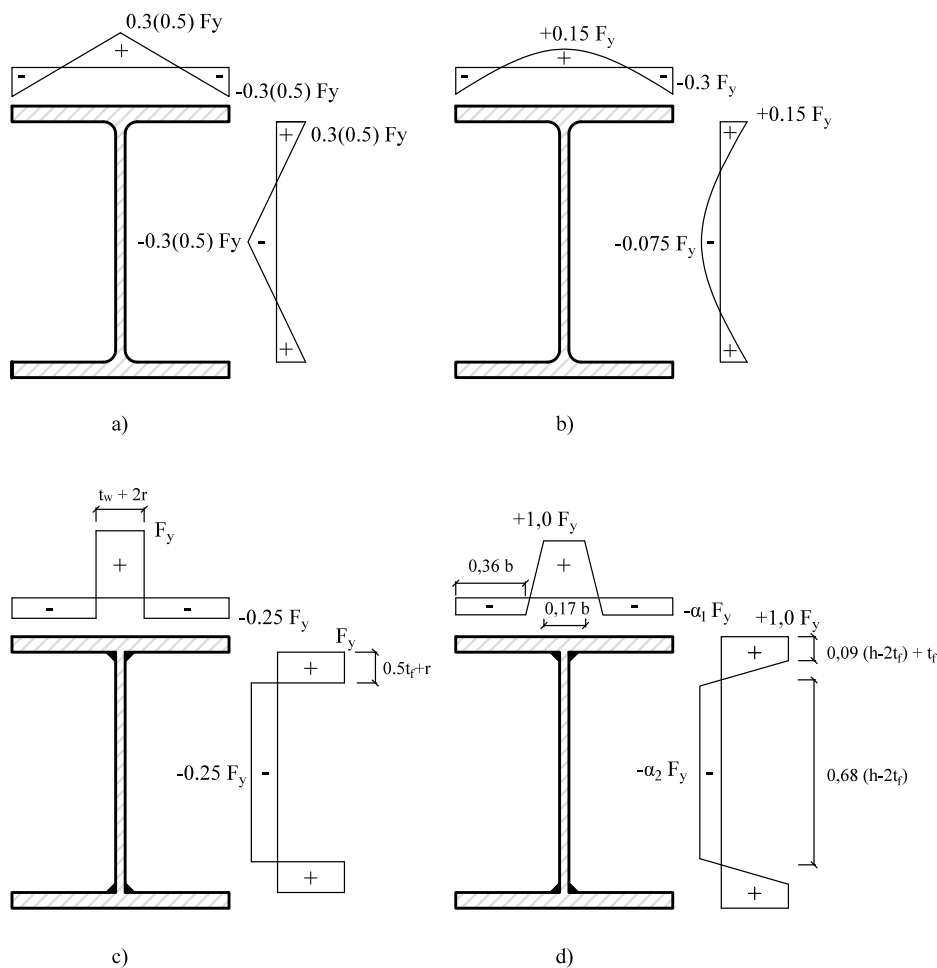


Figure 5: Residual stress patterns a) and b) concern hot-rolled sections whereas distributions c) and d) refer to welded sections residual stress pattern.

### 2.3 Geometrical imperfections

For the purpose to discern a reasonable reliable method to introduce imperfections into the FE model, investigations were performed with various sets of imperfections which are presented hereafter.

Geometrical imperfections were introduced into the FE model by means of appropriate modifications of nodes coordinates through adequate sinusoidal functions (see section 3.2 and 3.3) or using the 1<sup>st</sup> buckling mode shape (see section 3.4). The use of sinusoidal functions to introduce initial imperfections presents the advantage to allow greater control and command compared to the utilisation of the 1<sup>st</sup> eigenmode shape.

For each situation, several cases were considered. With respect to imperfections accounted for through sinusoidal functions, different amplitudes and periods were studied whereas according to the eigenmode imperfection, the variation of the amplitude was the single parameter differing between cases.

#### 2.3.1 Sinusoidal shapes

Figure 6 exhibits the three major cases encountered within the study which involves an initial imperfect shape obtained by modifications of nodes coordinates by means of sinusoidal functions.

In addition to vary in amplitude, the three patterns differ in their number of waves on the element. As a matter of fact, both the period and the number of waves on the member were modified between cases. The various sets of parameters used in the different cases are specified on Table 1. Figure 6 (a) refers to cases a), c) to i) whereas Figure 6 (b) represents the imperfection pattern on the flanges and web used in case b). Moreover, Figure 6 (c) enhances the imperfect shape of the web and flanges of case j).

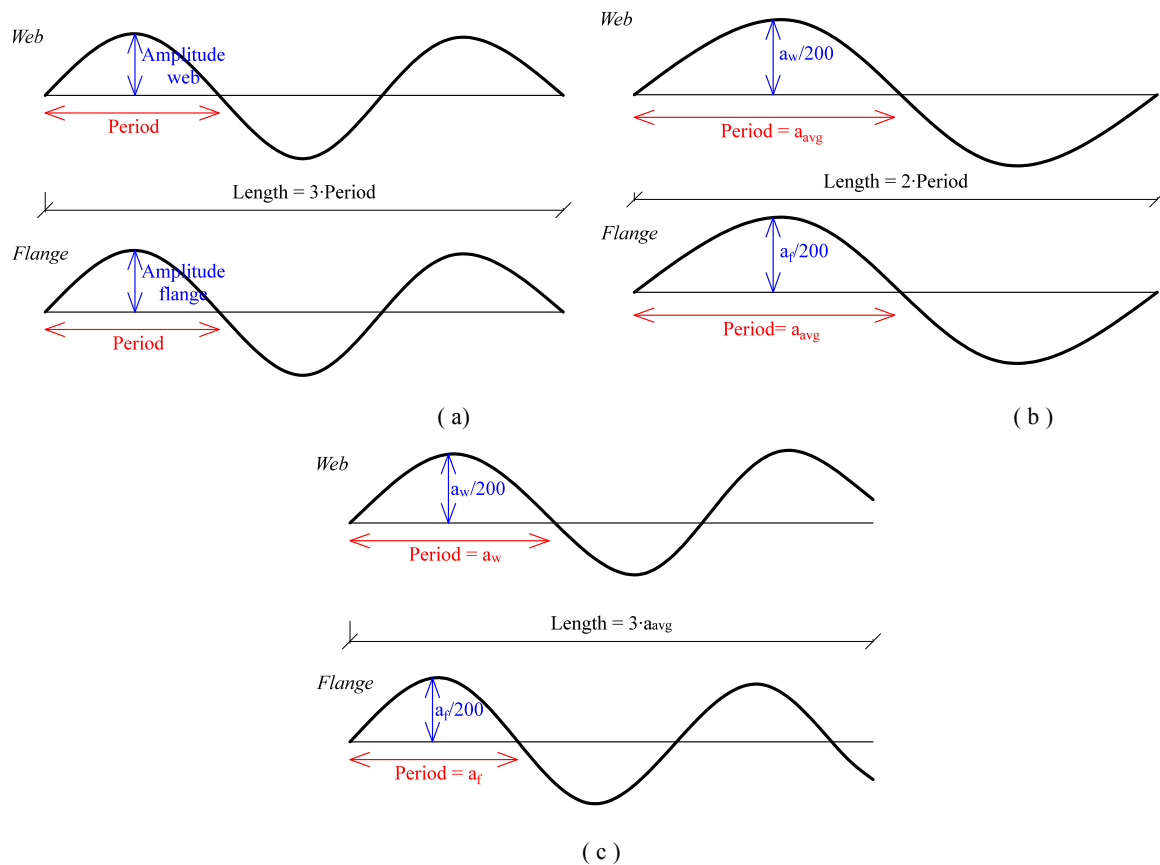


Figure 6: Description of input parameters in case of sinusoidal functions introduced as imperfections: (a) refers to cases a), c), d), e), f), g), h) and i) specified in Table 1; (b) refers to case b); (c) refers to case j).

As noted above, Table 1 summarizes the various sets of imperfections investigated throughout section 3.2 and 3.3. These parametric studies aim at providing a consistent database for comparison, to discern a reasonable pattern to recommend for FE modelling.

The name of each case presented in Table 1 describes the number of half-waves, the period of the half-wave and the amplitude of the sinusoid used to produce the initial deformed shape. Therefore, the case named  $3hw / P_{avg} / A_{pp\_200}$  contains an initial imperfect shape characterised by the presence of 3 half-waves, a half-wave period equal to the average between the web buckling length  $a_w$  and the flange buckling length  $a_f$ , and an amplitude applied respectively to each plate buckling length divided by 200. The flange and web buckling lengths differ according to the manufacturing process considered. With respect to hot-rolled sections,  $a_w = h - t_f - 2r$  and  $a_f = b - t_w - 2r$  where  $h$  refers to the whole height of the profile, whereas according to welded sections  $a_w = h - t_f$  and  $a_f = b$ .

Table 1: Definitions of the various cases considering the introduction of different types of imperfections studied and their associated parameters.

Case	Period	Amplitude web	Amplitude flange
a) $3hw / P_{avg} / A_{pp\_200}$	$a_{avg}$	$a_w/200$	$a_f/200$
b) $2hw / P_{avg} / A_{pp\_200}$	$a_{avg}$	$a_w/200$	$a_f/200$
c) $3hw / P_f / A_{pp\_200}$	$a_f$	$a_w/200$	$a_f/200$
d) $3hw / P_w / A_{pp\_200}$	$a_w$	$a_w/200$	$a_f/200$
e) $3hw / P_{avg} / A_{avg\_200}$	$a_{avg}$	$a_{avg}/200$	$a_{avg}/200$
f) $3hw / P_{avg} / A_f\_200$	$a_{avg}$	$a_f/200$	$a_f/200$
g) $3hw / P_{avg} / A_w\_200$	$a_{avg}$	$a_w/200$	$a_w/200$
h) $3hw / P_{avg} / A_{pp\_100}$	$a_{avg}$	$a_w/100$	$a_f/100$
i) $3hw / P_{avg} / A_{pp\_400}$	$a_{avg}$	$a_w/400$	$a_f/400$
j) $-hw / P_{pp} / A_{pp\_200}$	Period per plate	$a_w/200$	$a_f/200$

Table 2 and Table 3 present the resulting values of parameters specified in Table 1 for each I-section and H-section studied, respectively. These values are determined from the sections nominal dimensions.

Table 2: Values of the input parameters for each geometry of I-sections investigated throughout the parametric studies.

Case	Hot-rolled			Welded		
	IPE140	IPE400	IPES	IPE140	IPE400	IPES
$a_f$ [mm]	54.3	129.4	162	73	180	220
$a_w$ [mm]	112.2	331	714	133.1	386.5	781
$a_{avg}$ [mm]	83.25	230.2	438	103.05	283.25	500.5
$a_f/100$ [mm]	0.543	1.294	1.620	0.730	1.80	2.20
$a_w/100$ [mm]	1.122	3.310	7.140	1.331	3.865	7.81
$a_{avg}/100$ [mm]	0.834	2.302	4.380	1.031	2.833	5.005
$a_f/200$ [mm]	0.272	0.647	0.810	0.365	0.900	1.10
$a_w/200$ [mm]	0.561	1.655	3.570	0.666	1.933	3.905
$a_{avg}/200$ [mm]	0.416	1.151	2.190	0.515	1.416	2.503
$a_f/400$ [mm]	0.136	0.324	0.405	0.183	0.450	0.550
$a_w/400$ [mm]	0.281	0.828	1.785	0.333	0.966	1.953
$a_{avg}/400$ [mm]	0.208	0.576	1.095	0.258	0.708	1.251

Table 3: Values of the input parameters for each geometry of H-sections investigated throughout the parametric studies.

Case	Hot-rolled			Welded		
	HEA160	HEA600	HEAS	HEA160	HEA600	HEAS
$a_f$ [mm]	124	233	240	160	300	300
$a_w$ [mm]	104	486	226	143	565	290
$a_{avg}$ [mm]	114	359.5	233	151.5	432.5	295
$a_f/100$ [mm]	1.240	2.330	2.400	1.60	3.0	3
$a_w/100$ [mm]	1.040	4.860	2.260	1.43	5.65	2.90

$a_{avg}/100$ [mm]	1.140	3.595	2.330	1.515	4.325	2.95
$a_f/200$ [mm]	0.620	1.165	1.200	0.80	1.50	1.5
$a_w/200$ [mm]	0.520	2.430	1.130	0.715	2.825	1.45
$a_{avg}/200$ [mm]	0.570	1.796	1.165	0.758	2.163	1.475
$a_f/400$ [mm]	0.310	0.583	0.600	0.40	0.75	0.75
$a_w/400$ [mm]	0.260	1.215	0.565	0.358	1.413	0.725
$a_{avg}/400$ [mm]	0.285	0.899	0.583	0.379	1.081	0.738

Figure 7 exhibits the initial shape including amplified imperfections for the cases a), b) and j) described in Table 1. From left to right, the amplified initial shape enhances:

- 3 half-waves on the web and flanges and corresponds to case a) specified in Table 1;
- 2 half-waves on the web and flanges and corresponds to case b) specified in Table 1;
- approximately 2 half-waves on the web and 4 half-waves on the flanges and corresponds to case j) specified in Table 1.

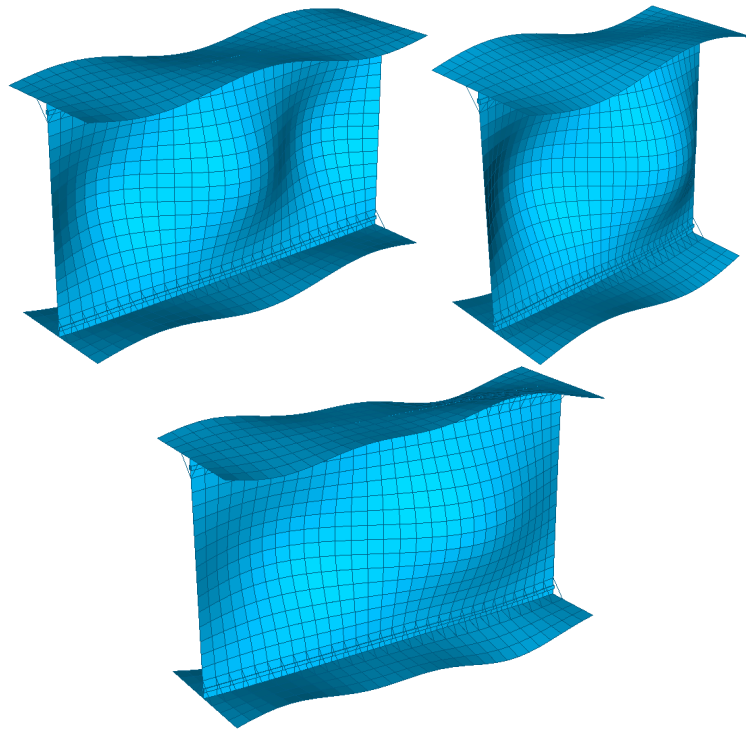


Figure 7: Magnified initial deformations of an axially compressed IPE 140; case a); case b); case j) from left to right.

### 2.3.2 Eigenmode shape

The use of the 1<sup>st</sup> buckling mode shape provided by linear buckling analysis (LBA) represents one of the most common method for the modelling of initial imperfections. Therefore, for each section considered, Table 5 and Table 6 point out the 1<sup>st</sup> eigenmode shape of I-sections and H-sections under pure compression and pure major axis-bending respectively. Table 4 specifies for each case studied the values of the amplification factor applied to magnify the deformed shape.

Table 4: Values of amplitudes applied to amplify the 1<sup>st</sup> buckling mode shape and considered within the parametric study.

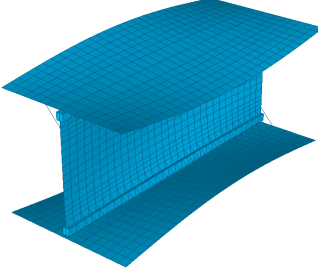
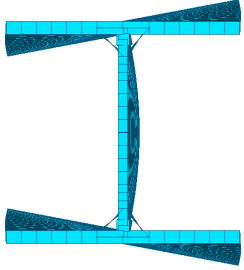
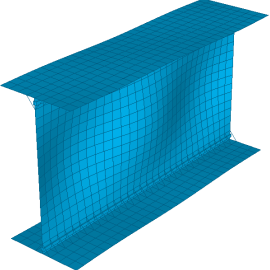
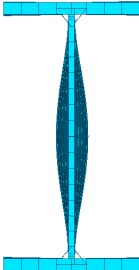
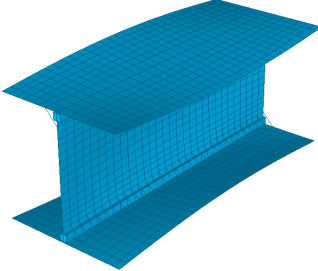
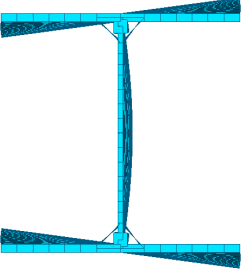
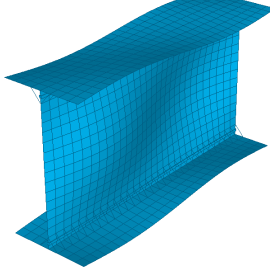
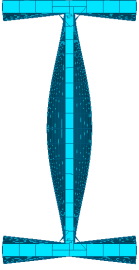
Case	Amplitude x	Amplitude y	Amplitude z
k) A avg 100	$a_{avg}/100$	$a_{avg}/100$	$a_{avg}/100$
l) A avg 200	$a_{avg}/200$	$a_{avg}/200$	$a_{avg}/200$
m) A avg 400	$a_{avg}/400$	$a_{avg}/400$	$a_{avg}/400$
n) A pp 100	$a_{avg}/100$	$a_w/100$	$a_f/100$
o) A pp 200	$a_{avg}/200$	$a_w/200$	$a_f/200$
p) A pp 400	$a_{avg}/400$	$a_w/400$	$a_f/400$

Although the introduction of the 1<sup>st</sup> buckling mode shape as initial geometrical imperfection represents a convenient approach to introduce imperfections into a FE model, it does not allow great adaptability with respect to the number or amplitude of half-waves enhanced by the element.

The eigenmode shape is highly dependent on the cross-section shape and on each plate slenderness. Under pure compression, I-sections present major half-waves on their web whereas H-sections eigenmodes enhance similar half-waves characteristics on their flanges and web. Furthermore, the 1<sup>st</sup> buckling mode shape is also sensitive to the loading applied since it leads the area affected by compressive stresses. Consequently, the eigenmode dependency on loading situation leads to additional computing requirements to obtain the initial deformed shape.

Therefore, the adoption of the 1<sup>st</sup> eigenmode as initial deformed shape presents the advantage to highlight and emphasize the section parts prone to undergo earlier buckling but the method enhances a lack of adaptability and requires additional numerical analyses.

Table 5: 1<sup>st</sup> eigenmode shape of the studied open-sections under pure compression.

HEA 160		
HEA 600		
HEAS		
IPE 140		

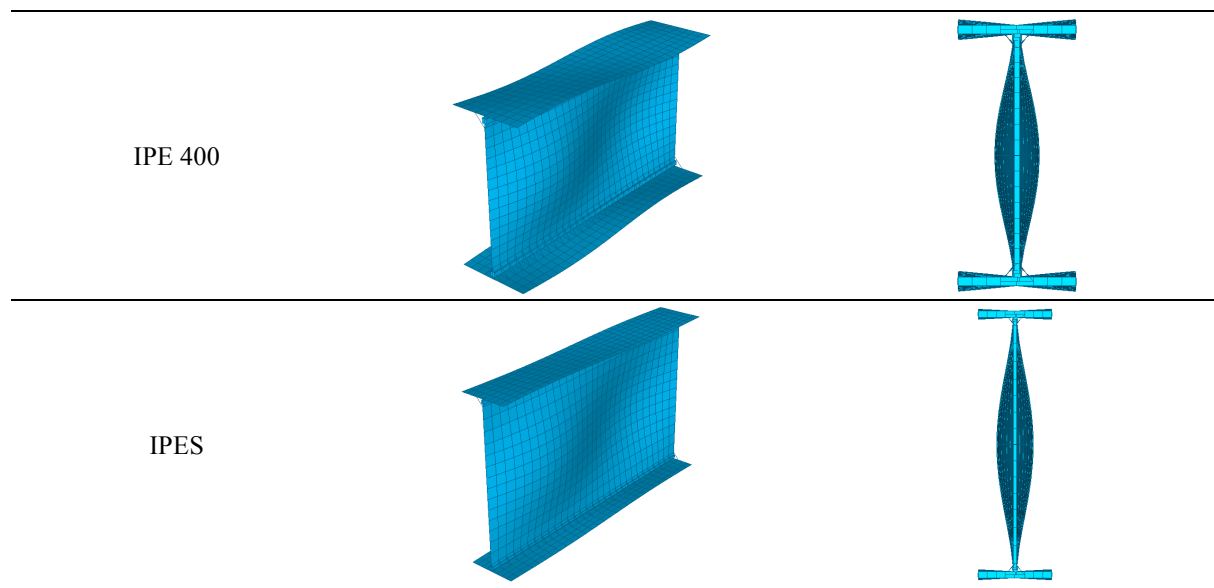
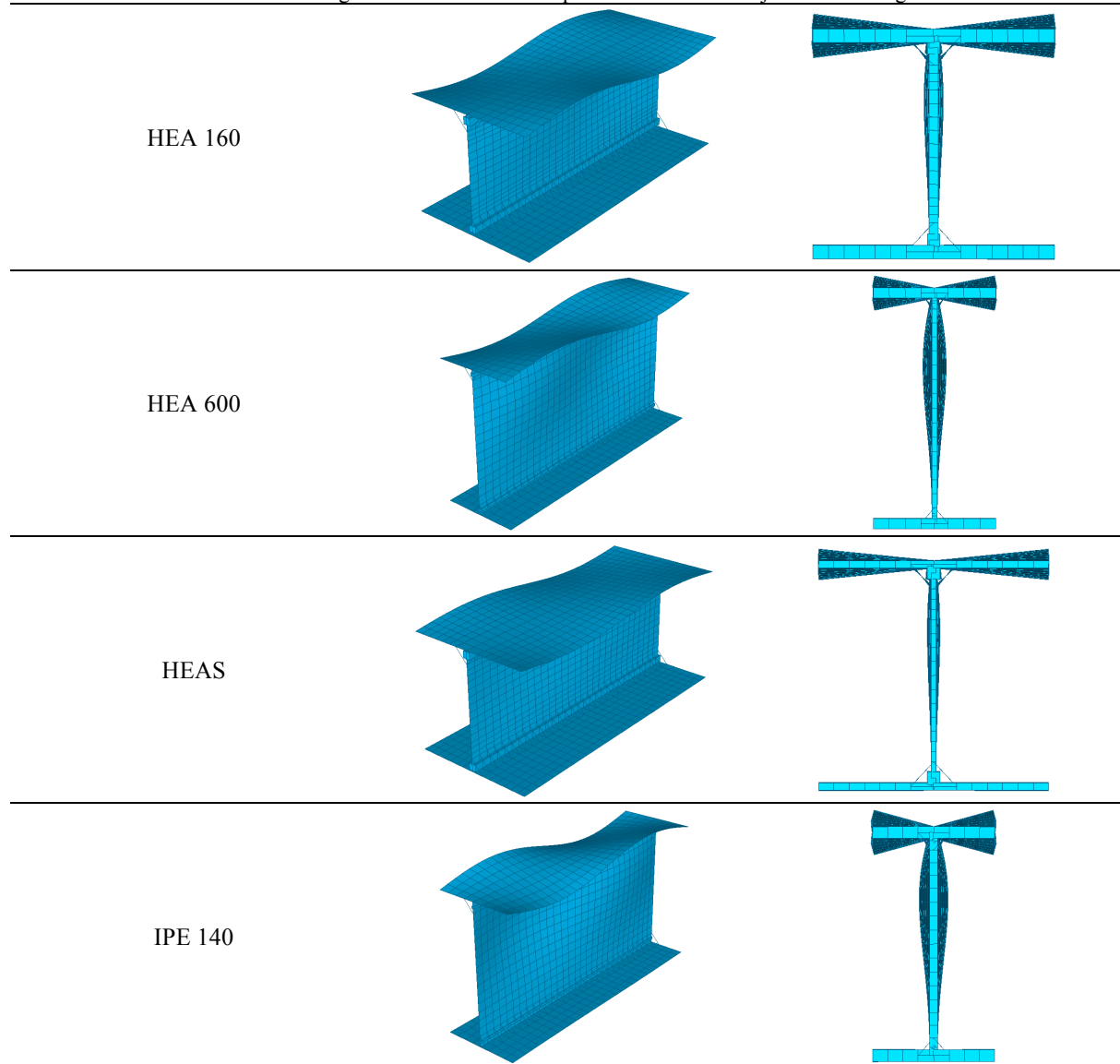
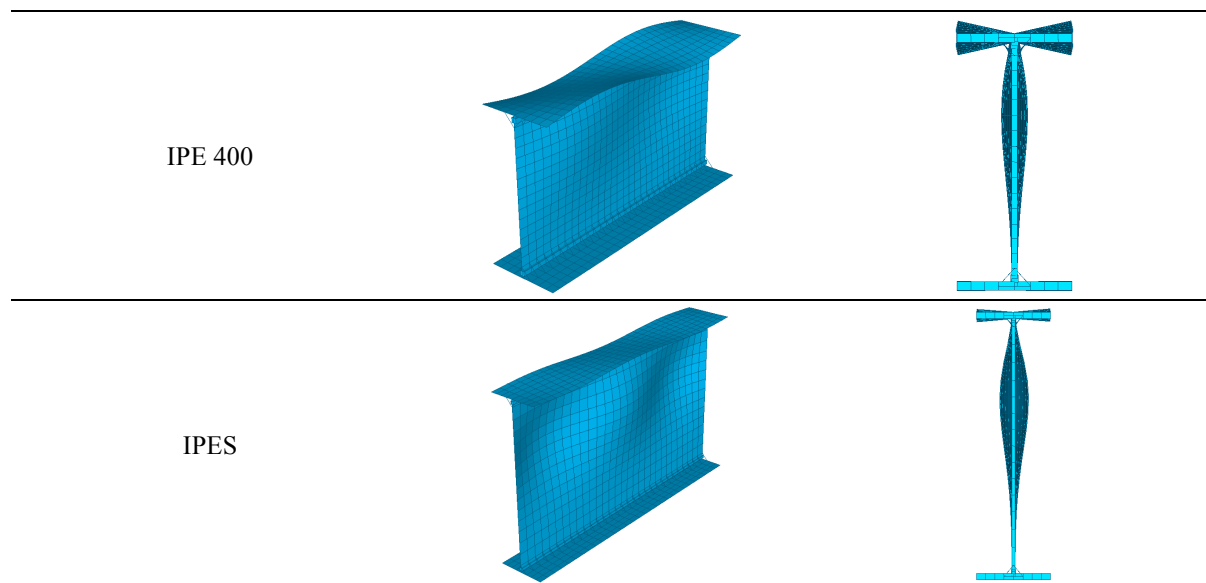


Table 6: 1<sup>st</sup> eigenmode of the studied open-sections under major-axis bending.





Consequently, with the FE model described above, numerical simulations were performed and results are presented within the subsequent sections. Section 3 concerns the influence of geometrical imperfections whereas section 4 presents the influence of material imperfections.

### 3 Influence of geometrical imperfections

The influence of initial geometrical imperfections is now studied throughout this first parametric study. As specified in section 2, several ways to introduce the initial deflected shape have been investigated and served as a basis to provide reasonable recommendations.

Section 3.1 presents a specific sub-study, which aims at procuring a comparison between experimental test results and ultimate resistance obtained with the sets of imperfections described in Table 1 and Table 4 of section 2. Then, section 3.2 exhibits the results respecting the investigation of geometrical imperfection amplitude influence on the ultimate resistance whereas section 3.3 addresses the effects of the half-wave period. Finally, the use of the 1<sup>st</sup> buckling mode shape as initial geometrical imperfection and the resulting load-carrying capacities are shown on section 3.4.

#### 3.1 Comparison with experimental results

A specific parametric study dedicated to the comparison between test results from a test campaign realised by Kettler (Kettler 2008) and FE simulation results is presented thereafter. All the specimens were hot-rolled except specimens A22-1, A22-2; A23-1, A23-2, A24-1 and A24-2 which were produced by welding. Numerical simulations were performed with the sets of imperfections specified in Table 1. Residual stresses were introduced through a parabolic and a trapezoidal residual stress pattern (see Figure 5) for hot-rolled and welded sections respectively.

The numerical simulations involve the same geometries as the ones investigated by Kettler, with the same sets of initial imperfections as specified in section 2. Table 7 exhibits the values of amplitudes and periods applied to the various plate elements. Moreover, Table 7 provides the real imperfections measured on the various specimens. These imperfections are procured in the form of maximal amplitudes measured along the web and flanges independently. However, since the reality of imperfections on the web was negligible, the web measured amplitude is set to 0 for all the specimens.

The comparison between the invented sets of amplitudes and the measured web and flanges maximum amplitudes points out that the maximal amplitudes measured on the flanges of the specimen tested at Graz University correspond to an amplitude of  $\frac{a_f}{100}$ .

Nevertheless, since the amplitudes provided coincide with the maximum encountered on the plate, the values do not highlight the overall behaviour of imperfections and further investigation is required. A detailed comparison between the ultimate load obtained from the test and the ultimate load-carrying capacity provided by numerical simulation will enable to procure a precise correlation between real amplitudes and reasonable initial imperfection to introduce into numerical simulations.

Table 7: Imperfection amplitude measured on the specimen tested as part of an experimental test campaign realised by Kettler and their corresponding set of amplitudes obtained from the measured geometry.

Specimen	Measured amplitudes			"Standard" sets of amplitudes (from measured geometry)								
	$a_{w, m}$ [mm]	$a_{f, m}$ [mm]	$a_{avg, m}$ [mm]	$a_w / 100$ [mm]	$a_f / 100$ [mm]	$a_{avg} / 100$ [mm]	$a_w / 200$ [mm]	$a_f / 200$ [mm]	$a_{avg} / 200$ [mm]	$a_w / 400$ [mm]	$a_f / 400$ [mm]	$a_{avg} / 400$ [mm]
sc_A1-2 $N+M_y$	0	3.2	1.6	1.79	<b>2.04</b>	<b>1.92</b>	0.90	1.02	0.96	0.45	0.51	0.48
sc_A1-3 $N+M_y$	0	3.2	1.6	1.80	<b>2.07</b>	<b>1.93</b>	0.90	1.04	0.97	0.45	0.52	0.48
sc_A2-1 $N+M_y+M_z$	0	3.4	1.7	1.80	<b>2.05</b>	<b>1.92</b>	0.90	1.03	0.96	0.45	0.51	0.48
sc_A2-2 $N+M_y+M_z$	0	3	1.5	1.80	<b>2.04</b>	<b>1.92</b>	0.90	1.02	0.96	0.45	0.51	0.48
sc_A3-1 $N+M_y+M_z$	0	3.5	1.75	1.80	<b>2.05</b>	<b>1.92</b>	0.90	1.03	0.96	0.45	0.51	0.48
sc_A3-2 $N+M_y+M_z$	0	3.1	1.55	1.80	<b>2.04</b>	<b>1.92</b>	0.90	1.02	0.96	0.45	0.51	0.48
sc_A4-1 $N+M_z$	0	3.6	1.8	1.80	<b>2.05</b>	<b>1.92</b>	0.90	1.03	0.96	0.45	0.51	0.48
sc_A4-2 $N+M_z$	0	3.1	1.55	1.80	<b>2.04</b>	<b>1.92</b>	0.90	1.02	0.96	0.45	0.51	0.48
sc_A10-2 $N+M_z$	0	2.8	1.4	1.80	<b>2.06</b>	1.93	0.90	1.03	<b>0.96</b>	0.45	0.51	0.48
sc_A5-1 $N$	0	2.9	1.45	1.79	<b>2.04</b>	<b>1.92</b>	0.90	1.02	0.96	0.45	0.51	0.48
sc_A5-2 $N$	0	2.8	1.4	1.79	<b>2.05</b>	1.92	0.90	1.02	<b>0.96</b>	0.45	0.51	0.48
sc_A7-1 $N+M_y$	0	4	2	1.82	<b>2.06</b>	<b>1.94</b>	0.91	1.03	0.97	0.46	0.52	0.49
sc_A7-2 $N+M_y$	0	3.8	1.9	1.82	<b>2.06</b>	<b>1.94</b>	0.91	1.03	0.97	0.46	0.52	0.49
sc_A1-1 $N+M_y$	0	3.8	1.9	1.82	<b>2.06</b>	<b>1.94</b>	0.91	1.03	0.97	0.46	0.51	0.49
sc_A8-1 $N+M_y+M_z$	0	4.4	2.2	1.82	<b>2.06</b>	<b>1.94</b>	0.91	1.03	0.97	0.46	0.52	0.49
sc_A8-2 $N+M_y+M_z$	0	3.2	1.6	1.82	<b>2.06</b>	<b>1.94</b>	0.91	1.03	0.97	0.46	0.52	0.49
sc_A9-1 $N+M_y+M_z$	0	3.5	1.75	1.82	<b>2.06</b>	<b>1.94</b>	0.91	1.03	0.97	0.46	0.52	0.49
sc_A9-2 $N+M_y+M_z$	0	5	2.5	1.82	<b>2.06</b>	<b>1.94</b>	0.91	1.03	0.97	0.46	0.52	0.49
sc_A10-1 $N+M_z$	0	5	2.5	1.82	<b>2.06</b>	<b>1.94</b>	0.91	1.03	0.97	0.46	0.52	0.49
sc_A10-3 $N+M_z$	0	2.8	1.4	1.82	<b>2.08</b>	1.95	0.91	1.04	<b>0.98</b>	0.46	0.52	0.49
sc_A11-1 $N$	0	4	2	1.85	<b>2.04</b>	<b>1.94</b>	0.92	1.02	0.97	0.46	0.51	0.49

sc_A11-2 $N$	0	4.4	2.2	1.85	<b>2.04</b>	<b>1.94</b>	0.92	1.02	0.97	0.46	0.51	0.49
sc_A22-1 $N+M_y$	0	3.5	1.75	2.34	<b>2.59</b>	2.47	1.17	1.30	<b>1.23</b>	0.59	0.65	0.62
sc_A22-2 $N+M_y$	0	3.1	1.55	2.34	<b>2.59</b>	2.47	1.17	1.30	<b>1.23</b>	0.59	0.65	0.62
sc_A23-1 $N+M_z$	0	3.5	1.55	2.34	<b>2.59</b>	2.47	1.17	1.30	<b>1.23</b>	0.59	0.65	0.62
sc_A23-2 $N+M_z$	0	3.2	1.6	2.34	<b>2.59</b>	2.47	1.17	1.30	<b>1.23</b>	0.59	0.65	0.62
sc_A24-1 $N$	0	2.4	1.2	2.34	<b>2.59</b>	2.47	1.17	1.30	<b>1.23</b>	0.58	0.65	0.62
sc_A24-2 $N$	0	2	1	2.35	<b>2.59</b>	2.47	1.17	1.30	<b>1.24</b>	0.59	0.65	0.62

Figure 8 to Figure 11 present a comparison between the ultimate load obtained from the experimental tests and the results provided by numerical simulations with various sets of imperfections (see Table 1 of section 2).

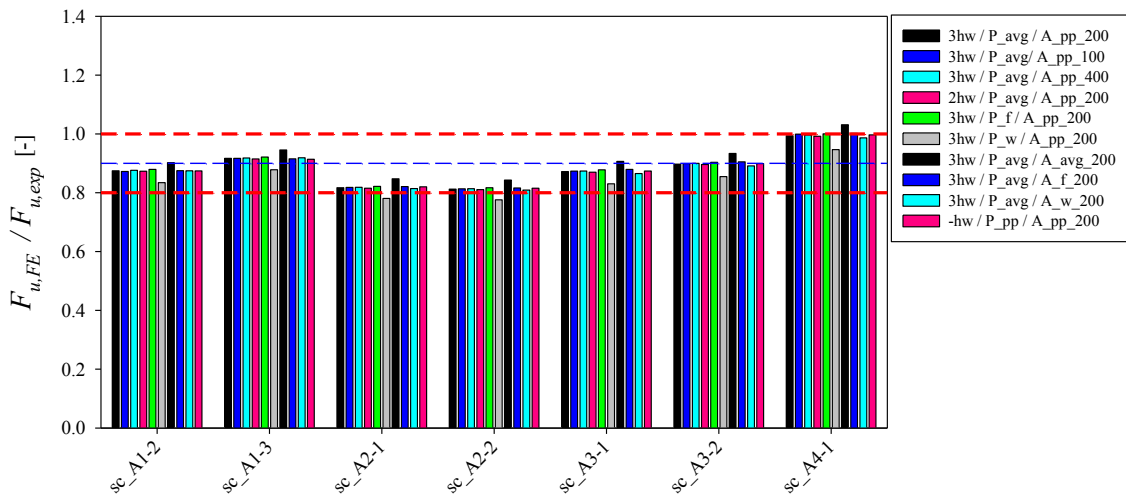


Figure 8: Ratio between ultimate load provided by numerical simulations with various geometrical imperfection types and their respective ultimate load procured by experimental test (Kettler 2008).

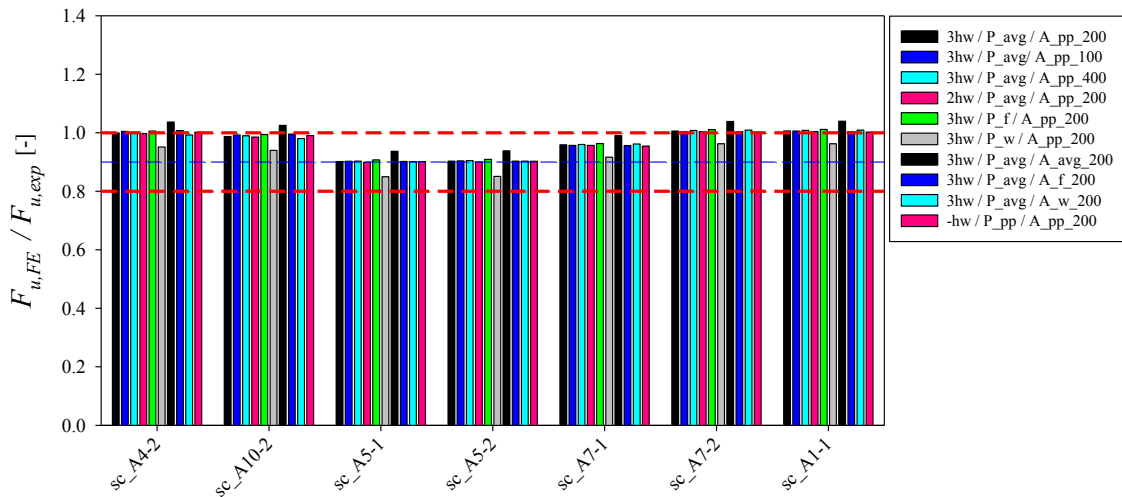


Figure 9: Ratio between ultimate load provided by numerical simulations with various geometrical imperfection types and their respective ultimate load procured by experimental test (Kettler 2008).

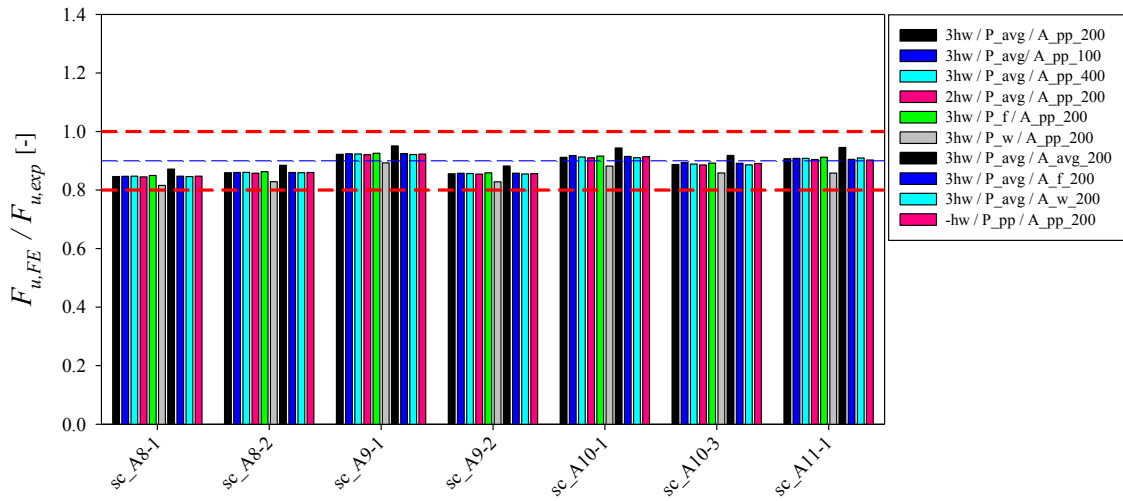


Figure 10: Ratio between ultimate load provided by numerical simulations with various geometrical imperfection types and their respective ultimate load procured by experimental test (Kettler 2008).

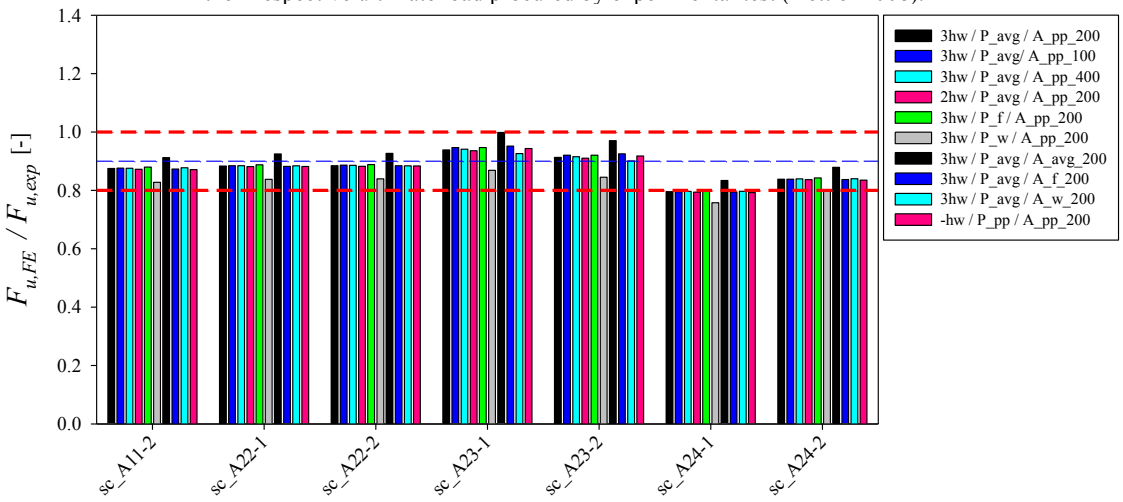


Figure 11: Ratio between ultimate load provided by numerical simulations with various geometrical imperfection types and their respective ultimate load procured by experimental test (Kettler 2008).

Figure 8 to Figure 11 reveal a great concordance between experimental results and FE simulations. As a matter of fact, by excluding the isolated results procured by cases  $3hw / P_{avg} / A_{avg\_200}$  and  $3hw / P_w / A_{pp\_200}$ ; 5 specimens reach 100% similarity between tests and FE results, 16 specimens enhance more than 90% of concordance and 12 specimens exhibit a ratio  $F_{u,FE}$  over  $F_{u,exp}$  situated between 80% and 90%.

All the sets of imperfections reach similar ultimate load capacities except 2 cases. Case  $3hw / P_{avg} / A_{avg\_200}$  leads to an overestimate of the ultimate resistance whereas case  $3hw / P_w / A_{pp\_200}$  procures the lowest ultimate resistance compared to the remaining sets of imperfections introduced. Therefore, the use of the average amplitude between  $a_w$  and  $a_f$  on both plates which reduces the imperfection on the governing larger plate appears to be over favourable.

This sub-study points out the reliability of the sets of imperfections adopted throughout the following parametric studies since an acceptable concordance between experimental and numerical results was achieved. From now on, deeper study on the effect of each set of imperfections will be presented.

### 3.2 Longitudinal wavelength

The influence of the number and period of the half-waves present on the member is investigated hereafter.

As specified in section 2 (Table 1), 5 cases with different half waves period characteristics are distinguished. They differ in their initial imperfect shape according to the number and period of the half-waves:

- $3hw / P_{avg} / A_{pp\_200}$ ;
- $3hw / P_f / A_{pp\_200}$ ;
- $3hw / P_w / A_{pp\_200}$ ;
- $-hw / P_{pp} / A_{pp\_200}$ ;
- $2hw / P_{avg} / A_{pp\_200}$ .

Cases  $3hw / P_f / A_{pp\_200}$  and  $3hw / P_w / A_{pp\_200}$  exhibit 3 half-waves along the member, as well as case  $3hw / P_{avg} / A_{pp\_200}$ . However, depending on the section dimensions, they result in various lengths in the FE models.

On the other hand, in case  $-hw / P_{pp} / A_{pp\_200}$ , the web and flanges enhance different number of half-waves and this number is not restrained to 3. Moreover, Case  $2hw / P_{avg} / A_{pp\_200}$  exhibits 2 half-waves regardless of the section considered.

According to the various cases characteristics, observations regarding the influence of the number of half-waves can be made from results obtained with  $3hw / P_{avg} / A_{pp\_200}$  case with the ones obtained with  $-hw / P_{pp} / A_{pp\_200}$  and  $2hw / P_{avg} / A_{pp\_200}$  cases also.

The x-axis on Figure 12 and Figure 13 refers to the local slenderness  $\lambda_L$  characterising the ratio between the section full plastic resistance and its behaviour against pure stability. On the other hand, the y-axis represents the local reduction factor  $\chi_L$ , which, applied to the full plastic capacity, leads to the cross-sectional ultimate resistance (Boissonnade, et al. 2017). The  $\chi_L$ - $\lambda_L$  figures contain the following reference curves:

- the horizontal dashed line,  $\chi_L = 1$  which refers to the full plastic resistance;
- the parabolic dashed line,  $\chi_L = 1/\lambda_L$  describing Von Karman equation for the local critical buckling load of an ideal elastic element free of imperfections;
- Winter curve dedicated to plate buckling and based on experimental tests;
- Kettler curve (Kettler 2008) resulting from a study on the plastic capacity of semi-compact H-sections.

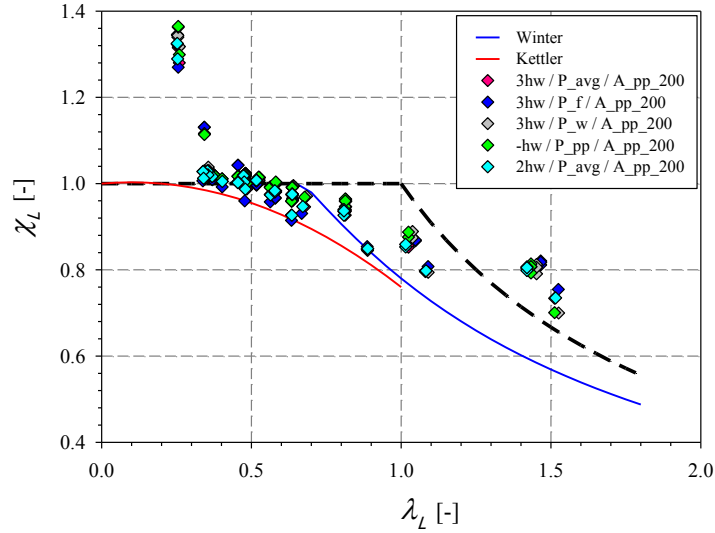


Figure 12: Results from numerical simulations on I sections under pure compression and pure major-axis bending, using a sinusoidal imperfection with variation in the period of the longitudinal buckling wave.

The most slender sections shown on Figure 12 and presenting a local slenderness  $\lambda_L = 1.50$ , exhibit a local reduction factor higher than the elastic behaviour of a perfect plate described by Von Karman curve  $\chi_L = 1/\lambda_L$ . As a matter of fact, Von Karman equation describes the behaviour of an ideal elastic plate and therefore the interaction between plates enhanced on the cross-sectional behaviour is not taken into account (Li 2014).

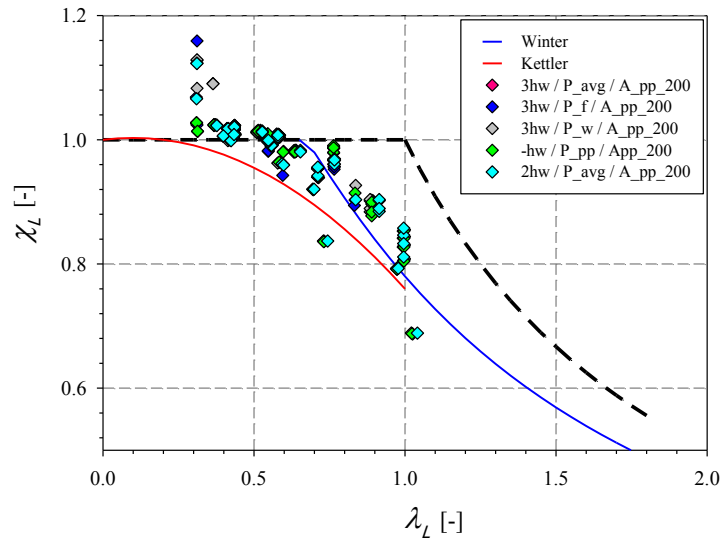


Figure 13: Results from numerical simulations on H sections under pure compression and pure major-axis bending, using a sinusoidal imperfection with variation in the period of the longitudinal buckling wave.

The analysis of Figure 12, Figure 13 and Figure 14 leads to the following observations:

- At low slenderness, on Figure 12 and Figure 13, results lie above the pure resistance limit with  $\chi_L \geq 1.0$ . However, since these results were obtained at a state of large deformations, they enhanced important influence of strain-hardening.
- As shown on Figure 12, Figure 13 and Figure 14, results obtained with 2 half-waves reach sensitively the same resistance as the results provided by the case which exhibit 3 half-waves when a similar half-wave period is considered.
- Figure 12 points out a peculiarity according to the influence of the length of the section for numerical simulations performed on *IPES* section. As a matter of fact, this section exhibits the minimum ratio  $b/h = 0.28$ . Thus, when the flange width is used as the period of the half-wave, it decreases the length of the element to obtain 3 half-waves

on the element and an increased strength is obtained, which is attributed to the influence of boundary conditions providing additional stiffness.

- Isolated results located below Kettler curve are highlighted on Figure 13 at  $\lambda_L = 1.024$  and  $\lambda_L = 0.736$ , which correspond to numerical simulations performed with a welded residual stress pattern. Therefore, the important drop in resistance can be due to a severe residual stress applied initially.

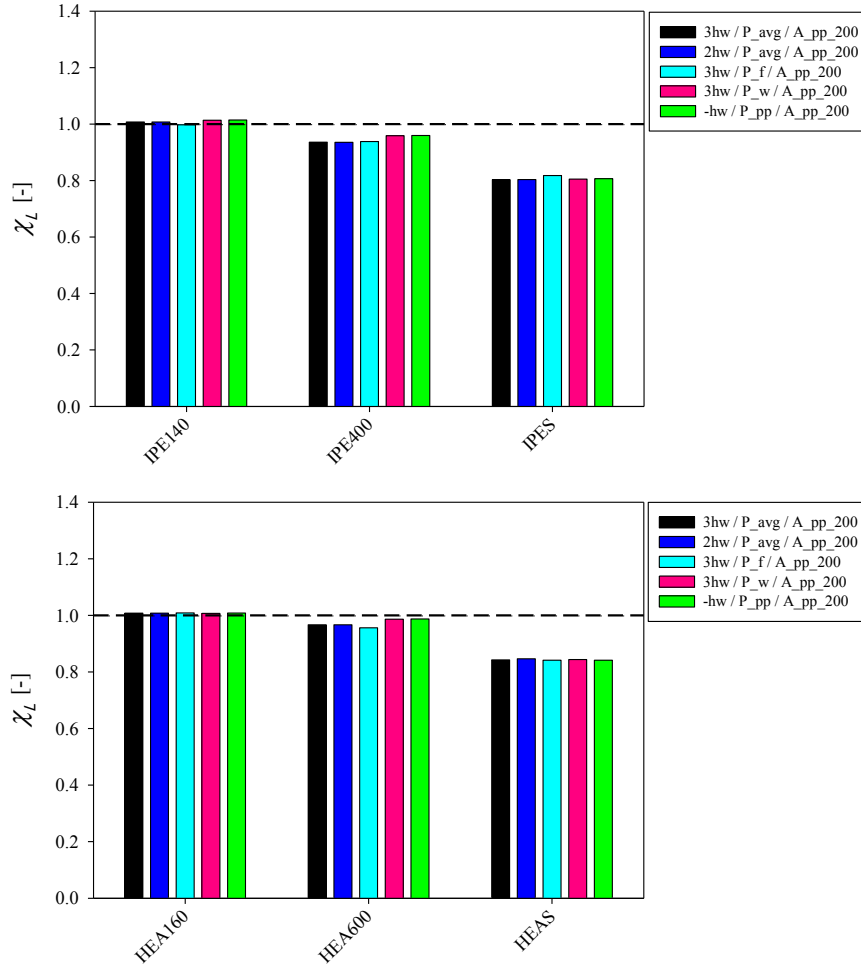


Figure 14: Histograms which enhance the influence of the period of the sinusoidal imperfection on I-sections (upper histogram) and H-sections (lower histogram) made of steel S460, under axial compression.

Figure 14 highlights that case  $-hw / P_{pp} / A_{pp\_200}$  can result in increased resistance. This set of imperfections involves the presence of different number of half-waves in the web and flanges. Besides, since the length of the specimen was chosen equal to the length obtained with case  $3hw / P_{avg} / A_{pp\_200}$ , the element does not necessarily enhance whole half-waves, which can decrease the second order effects.

However, as shown on Figure 14, the discrepancy between results is insignificant and, does not reflect leads for choosing a specific period for the sinusoidal function introduced to modify the nodes position of the element.

### 3.3 Amplitude of local geometrical default

Secondly, to pursue the investigation of the influence of geometrical imperfections on the ultimate local resistance of open-sections, the subsequent section gathers the results and resulting observations related to the influence of the amplitude of the initial imperfections. The characteristics of the following 6 cases investigated hereafter, which differ in the amplitude of the half-waves are specified in section 2 (Table 1):

- $3hw / P_{avg} / A_{pp\_100}$ ;
- $3hw / P_{avg} / A_{pp\_200}$ ;
- $3hw / P_{avg} / A_{pp\_400}$ ;
- $3hw / P_{avg} / A_{avg\_200}$ ;
- $3hw / P_{avg} / A_w\_200$ ;
- $3hw / P_{avg} / A_f\_200$ .

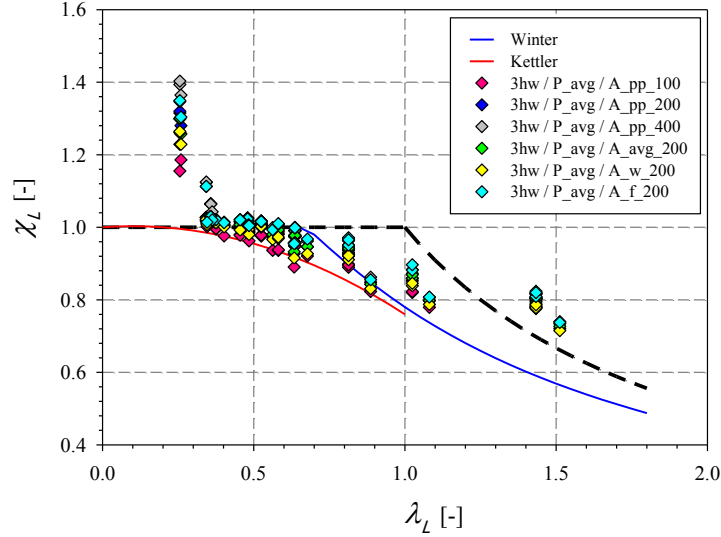


Figure 15: Results from numerical simulations on I sections under pure compression and pure major-axis bending, using a sinusoidal imperfection with variation in the amplitude of the longitudinal buckling wave.

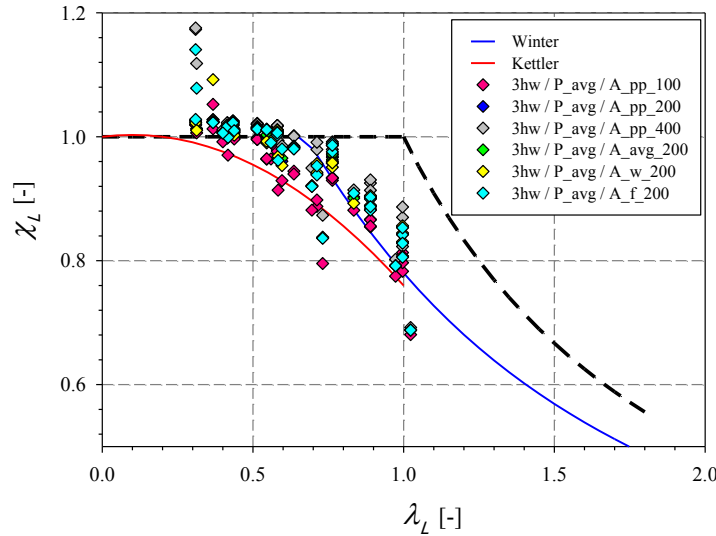


Figure 16: Results from numerical simulations on H sections under pure compression and pure major-axis bending, using a sinusoidal imperfection with variation in the amplitude of the longitudinal buckling wave.

As expected, Figure 15, dedicated to the behaviour of I-sections highlights lower resistance when the length of the web governs the amplitude of the imperfection ( $3hw / P_{avg} / A_w\_200$ ) instead of the flange width ( $3hw / P_{avg} / A_f\_200$ ). This trend was foreseeable since I-sections exhibit a ratio  $b/h < 1$ .

Moreover, for all loading situations, yield stress employed and residual stress pattern used, section *HEA160* which presents a ratio  $b/h > 1$ , enhances higher resistance for case  $3hw / P_{avg} / A_w\_200$  where the web height is used for the amplitude of the imperfection compared to case  $3hw / P_{avg} / A_f\_200$  in which the flange width is employed (see Figure 16 and Figure 17). As a matter of fact, this section flange width is higher than its web height, and, therefore,

the imperfection  $A_w_{200}$  related to the web provides higher resistance than  $A_f_{200}$  which depends on the flange width.

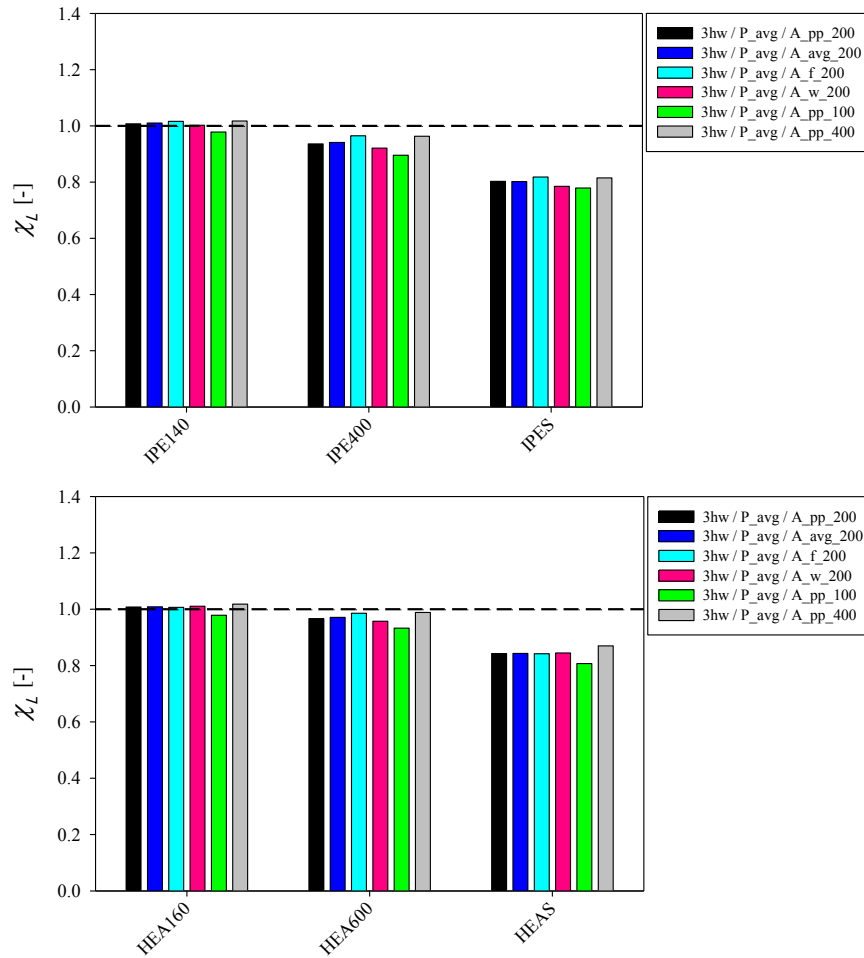


Figure 17: Histograms which enhance the influence of the amplitude of the sinusoidal imperfection on I-sections (upper histogram) and H-sections (lower histogram) made of steel S460, under axial compression.

With respect to an amplitude chosen respectively to each plate, all figures highlight the obtainment of lower resistances for increased amplitude such as  $A_{pp\_100}$  case compared to lower amplitudes applied such as  $A_{pp\_200}$  and  $A_{pp\_400}$ . Differences up to 7% between  $3hw / P_{avg} / A_{pp\_100}$  and  $3hw / P_{avg} / A_{f\_400}$  are observed on Figure 17.

Moreover, Figure 17 enhances that similar ultimate local load-carrying resistance are provided for an amplitude chosen respectively to each plate  $A_{pp\_200}$  and results obtained with a similar amplitude applied to each plate corresponding to  $A_{avg\_200}$ .

### 3.4 Eigenmode - conform initial pattern

Ultimately, the influence of the amplification applied to the 1<sup>st</sup> buckling mode shape is developed herein. Both plate per plate and overall amplitudes were studied with various factors considered.

The cases  $A_{pp\_100}$ ,  $A_{pp\_200}$  and  $A_{pp\_400}$  consider an amplification factor  $a_i$  which differs within the plates ( $a_w$  and  $a_f$  on the web and flanges respectively), whereas respecting to cases  $A_{avg\_100}$ ,  $A_{avg\_200}$  and  $A_{avg\_400}$ , the same amplification factor is applied on the three plates and corresponds to the average between  $a_f$  and  $a_w$ .

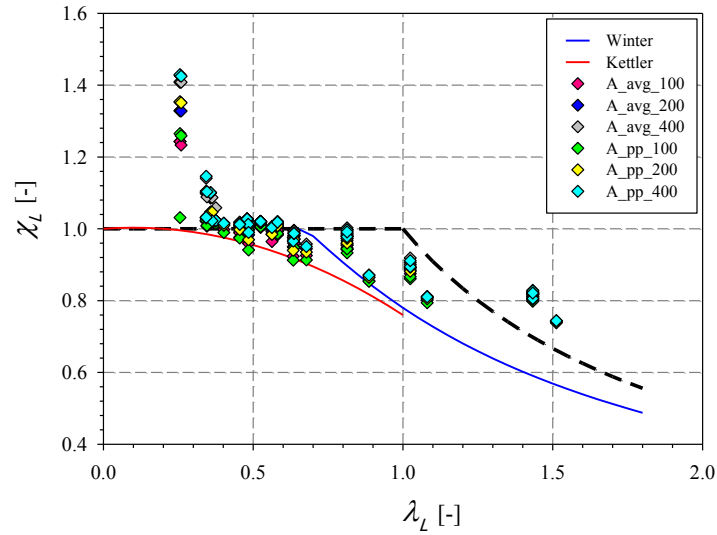


Figure 18: Results from numerical simulations on I sections under pure compression and pure major-axis bending, using the 1<sup>st</sup> eigenmode as initial imperfection with variation in the amplitude applied to magnify the 1<sup>st</sup> buckling mode shape.

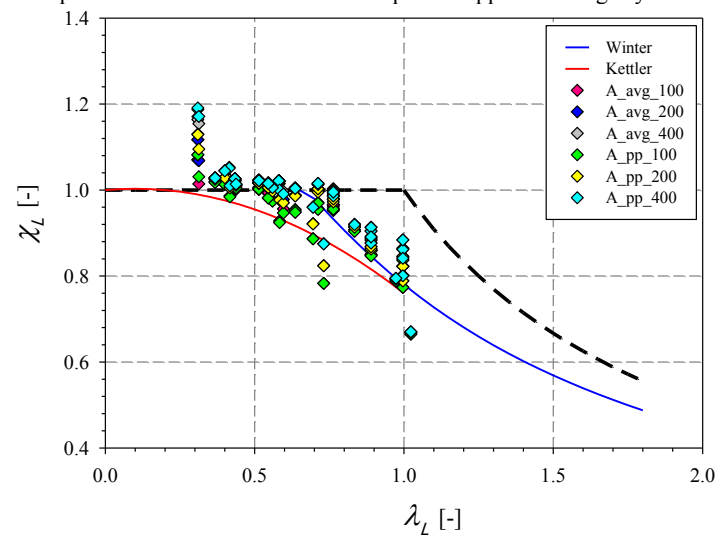


Figure 19: Results from numerical simulations on H sections under pure compression and pure major-axis bending, using the 1<sup>st</sup> eigenmode as initial imperfection with variation in the amplitude applied to magnify the 1<sup>st</sup> buckling mode shape.

Figure 18 and Figure 19 point out that the lowest ultimate resistance is obtained for  $A_{pp\_100}$  and the highest ultimate resistance with an amplitude  $A_{pp\_400}$ , with respect to the plate-per-plate applied amplitude. Similar results are expected for an average amplitude  $A_{avg\_i}$  which is verified on Figure 20.

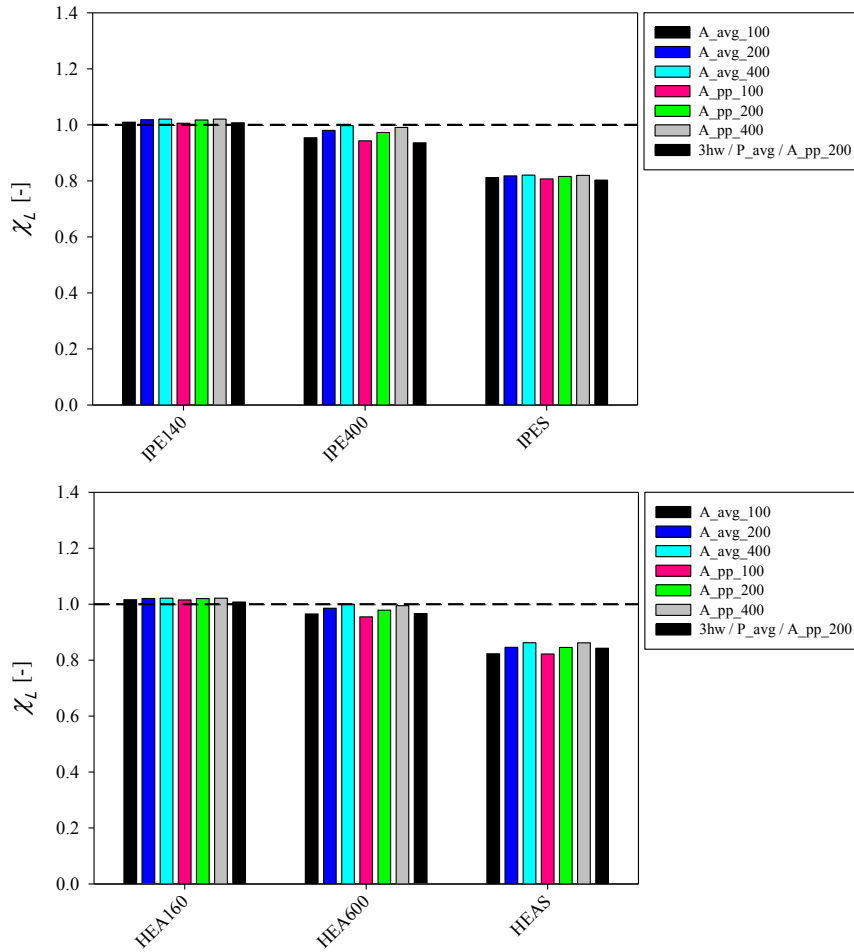


Figure 20: Histograms which enhance the influence of the amplitude of amplification applied on the 1<sup>st</sup> buckling mode shape on I-sections (upper histogram) and H-sections (lower histogram) made of steel S460, under axial compression.

Whether if an average amplitude is applied overall or if the amplitude is applied independently with respect to each plate buckling length, the 3 figures above display similar results between the same order of amplitude, e.g  $A_{avg\_100}$  and  $A_{pp\_100}$ , even for I-sections which exhibit important differences in their web and flanges dimensions.

Furthermore, the use of the 1<sup>st</sup> buckling mode shape amplified with an amplitude divided by 100 ( $A_{avg\_100}$  and  $A_{pp\_100}$ ) leads to similar resistances than case  $3hw / P_{avg} / A_{pp\_200}$ , where a sinusoidal function is used to modify the nodes coordinates. Therefore, the use of the 1<sup>st</sup> eigenmode appears to be more favourable.

Nevertheless, even though residual stresses were included into the FE model used for the acquirement of results shown above, the sub-study described in section 3 is focused on the geometrical imperfections influence. Therefore, section 4 presents the study related to the influence of material imperfections on the local load-carrying capacity of I and H sections.

#### 4 Influence of material imperfections

The second parametric study presented in the following concerns the influence of material imperfections on the local ultimate load capacity of open-sections. The purpose of this study is to investigate the effects of various residual stress shapes for hot-rolled and welded sections to, at the end, suggest reliable guideline for FE modelling of material imperfections.

Therefore, both welded and hot-rolled sections were considered and residual stress patterns coming from each manufacturing process were introduced before loading was applied.

Moreover, with respect to hot-rolled sections, the influence of the maximum residual stress employed was investigated. Section 4.1 concerns hot-rolled sections whereas investigation respecting welded sections is presented on section 4.2.

#### 4.1 Hot-rolled profiles

Firstly, the influence of hot-rolled residual stress pattern on the local load-carrying capacity was studied. Moreover, the impact of the maximum residual stress used is presented hereafter. *triangular\_F<sub>y</sub> 235* and *triangular\_F<sub>y</sub> actual* refer to the triangular residual stress pattern whereas *parabolic\_F<sub>y</sub> 235* and *parabolic\_F<sub>y</sub> actual* are related to the parabolic pattern, which are both presented in Figure 5. Moreover, *F<sub>y</sub> actual* refers to residual stress patterns where a maximum stress corresponding to the actual yield limit have been used whereas *F<sub>y</sub> 235* concerns sections whose maximum residual stress corresponds to 235 MPa.

First, the local behaviour of I-sections and H-sections under various hot-rolled residual stress patterns for all cases of geometrical imperfections is presented within Figure 21 and Figure 22, respectively. The x-axis refers to the local slenderness  $\lambda_L$  whereas the y-axis represents the local reduction factor  $\chi_L$  (Boissonnade, et al. 2017).

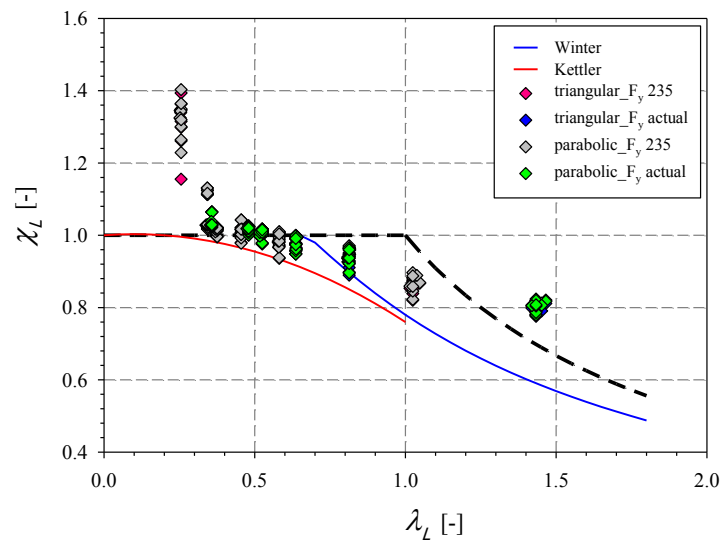


Figure 21: Results from numerical simulations on I sections under pure compression and pure major-axis bending, using various types of hot-rolled residual stress pattern.

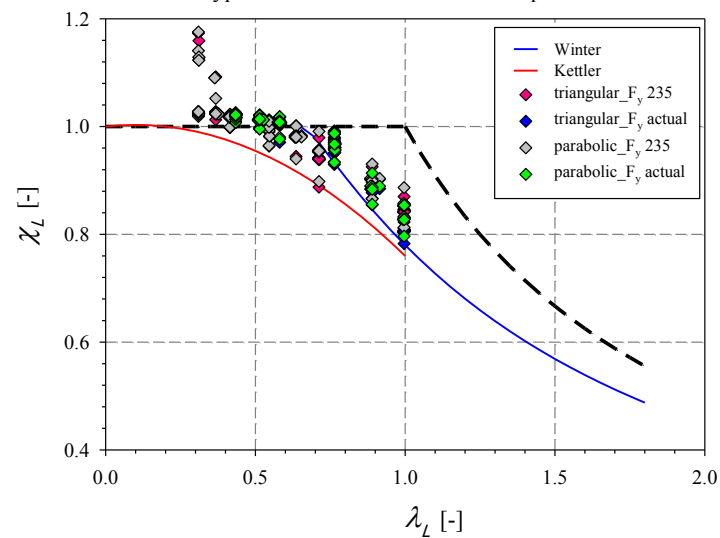


Figure 22: Results from numerical simulations on H sections under pure compression and pure major-axis bending, using various types of hot-rolled residual stress pattern.

As shown on Figure 21 and Figure 22, compact sections enhance lower discrepancy depending on the different residual stress patterns introduced, which can be explained by their lower sensitivity to imperfections. Figure 22 exhibits an important discrepancy in the results for H sections with a slenderness  $\lambda_L = 1.0$ , and belonging to the intermediate range. This disparity is due to the influence of both the residual stress chosen and the variations in the initial geometrical imperfections. Furthermore, results obtained for each residual stress pattern for very slender sections such as *IPES* with  $\lambda_L = 1.45$ , display negligible difference since this range of slenderness is less sensitive to the presence of imperfections.

Then, in addition, Figure 23 exhibits through a histogram the numerical results obtained for each residual stress pattern with a specific geometrical imperfection corresponding to case a)  $3hw / P_{avg} / A_{pp\_200}$  specified above. Figure 23 represents for each specimen studied, the corresponding local reduction factor procured for the pure compression case and plotted on the y-axis. The figure aims at highlighting the variations between results.

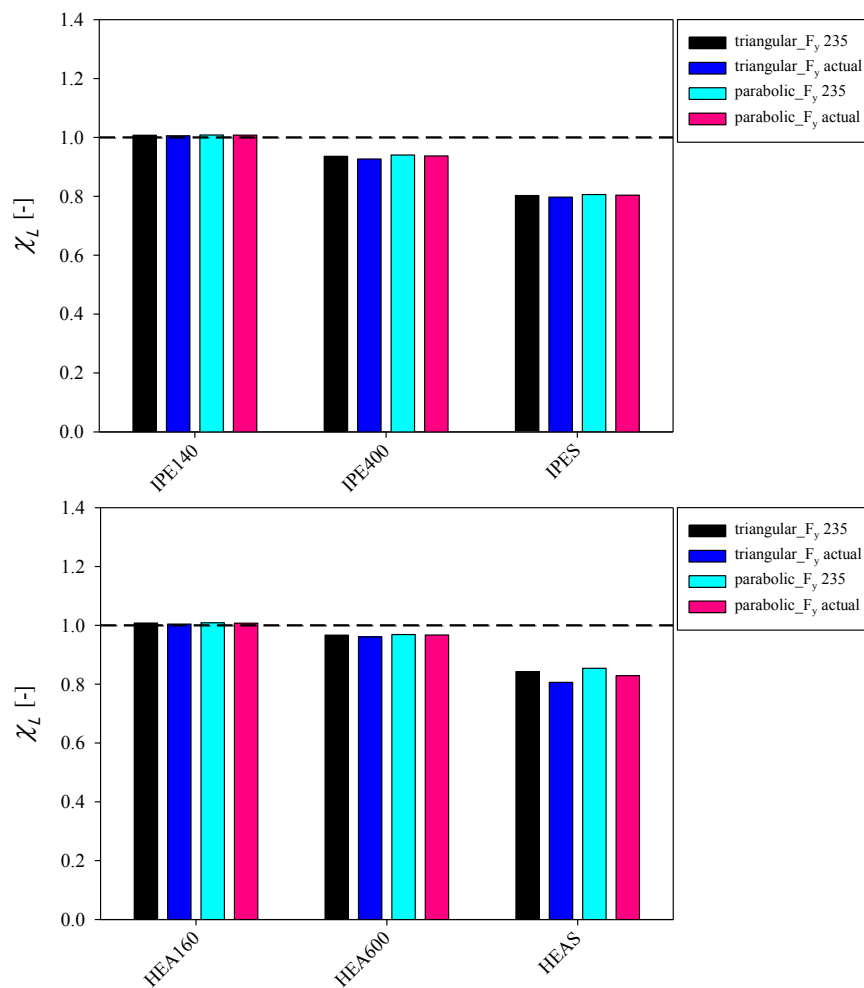


Figure 23: Histograms which enhance the influence of the hot-rolled residual stress pattern on I-sections (on the left) and H-sections (on the right) made of steel S460.

As expected, Figure 23 points out that when the actual yield limit is used instead of  $F_y = 235 \text{ MPa}$ , for sections made of  $F_y = 460 \text{ MPa}$ , a lower resistance is observed. As a matter of fact, regarding sections made of  $F_y = 460 \text{ MPa}$ , if the maximum residual stress achieved corresponds to  $460 \text{ MPa}$ , some fibres have already reached their plastic limit before loading is applied, and, hence, yielding spreads quicker involving earlier buckling and ultimately, failure. Therefore, for a similar ultimate strain allowed, compact sections whose applied

residual stress pattern is made with  $F_y = 460 \text{ MPa}$  will reach lower ultimate strength than the one with residual stress pattern made with  $F_y = 235 \text{ MPa}$ .

With respect to intermediate sections such as *IPE400* and *HEAS* under pure compression, since higher residual stresses induce earlier yielding and thus premature buckling, failure occurs at an early stage. However, for *HEAS* section the differences between results obtained are 3% and 4.5% lower for the parabolic and triangular shapes respectively, and 0.3% and 1% lower according to *IPE400*.

Moreover, Figure 23 enables to observe that the parabolic residual stress pattern seems to procure higher resistance than the triangular residual stress pattern, especially within sections of intermediate slenderness such as *IPE400* and *HEAS*. As a matter of fact, the influence of the variation in the residual stress pattern is more pronounced since this range of slenderness is more sensitive to the presence of imperfections. A worst residual stress pattern introduced into the model affects the occurrence of yielding and buckling which are both involved into the failure of sections of intermediate slenderness.

Nevertheless, these differences between the 2 residual stress patterns are 1.4% when  $F_y = 235 \text{ MPa}$  is used and 0.7% when  $F_y = 460 \text{ MPa}$  is employed, according to *HEAS* section. On the other hand, results provided with *IPES* exhibit a difference of 0.5% with  $F_y = 235 \text{ MPa}$  and 1.1 % with  $F_y = 460 \text{ MPa}$ .

To conclude, the discrepancy exhibited on Figure 21, Figure 22 and Figure 23 is insignificant and the adoption of a specific residual stress pattern for hot-rolled sections between the 2 studied herein is not evident. Both residual stress shapes provide reliable ultimate resistance. Moreover, with respect to the maximum residual stress used, since negligible differences were enhanced and no references in literature justify the attainment of the yield stress for hot-rolled sections, the use of  $F_y = 235 \text{ MPa}$  represents the most reasonable option.

#### 4.2 Welded sections

The influence of 2 residual stress patterns dedicated to welded sections and described in Figure 5 is studied hereafter. Again plotted in  $\chi - \lambda$  axes, Figure 24 and Figure 25 exhibit the results obtained from numerical simulations on welded I-sections and H-sections respectively. Afterwards, histograms presenting the results acquired for welded sections respecting to a specific case of geometrical imperfections (case *a*)  $3hw / P_{avg} / A_{pp\_200}$ ) are shown in Figure 26. *constant* refers to the sections whose residual stress pattern corresponds to the constant pattern suggested in Figure 5 whereas *trapezoidal* is related to the trapezoidal residual stress pattern. For both patterns, a maximum residual stress corresponding to the actual yield limit was considered since residual stresses as high as the yield limit are usually reached in the welded areas.

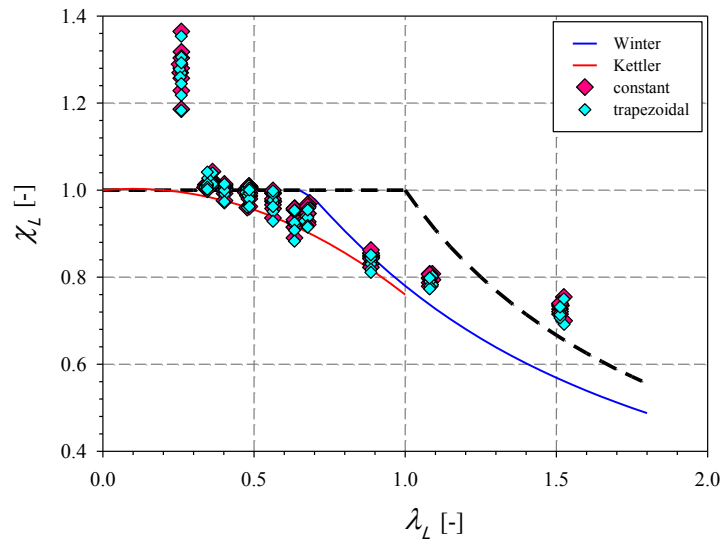


Figure 24: Results from numerical simulations on I sections under pure compression and pure major-axis bending, using various types of welded residual stress pattern.

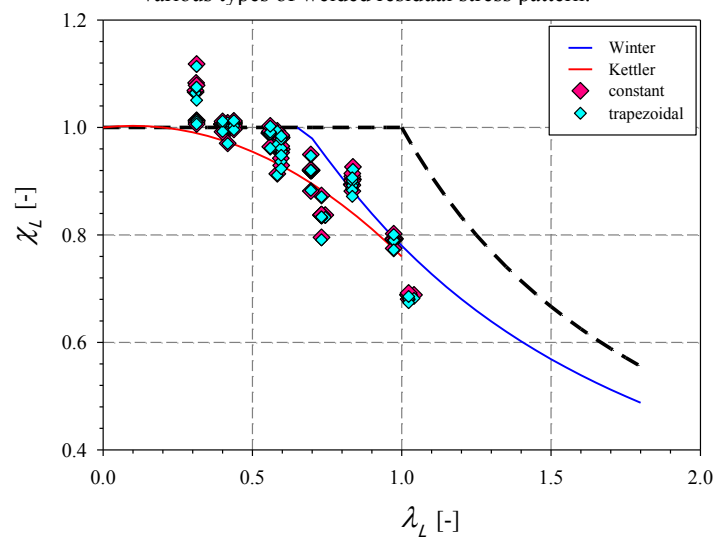


Figure 25: Results from numerical simulations on H sections under pure compression and pure major-axis bending, using various types of welded residual stress pattern.

Albeit no differences between results obtained with the *constant* and *trapezoidal* residual stress patterns are highlighted on Figure 25, Figure 24, related to the behaviour of welded I-sections, enhances a slight increased disparity among results.

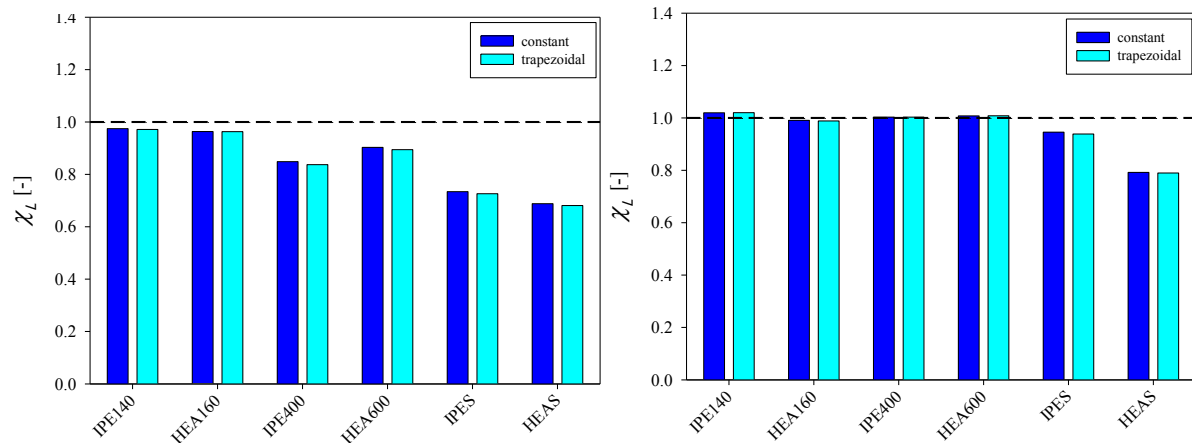


Figure 26: Histograms which enhance the influence of the welded residual stress pattern on I and H sections made of steel S460 under axial compression (on the left) and under major axis bending (on the right).

As shown on Figure 26, sections under pure compression procure lower resistance than sections under major axis bending, which was foreseen. The histograms point out that even though a minor difference between results is provided for the intermediate section *IPE400* under pure compression, which enhances a lower resistance procured with the trapezoidal residual stress pattern, the resistance reached with both residual stress patterns is notably similar.

## 5 Recommendations for the introduction of imperfections in FE modelling

By means of an extensive campaign of numerical simulations on I and H sections, the investigations regarding the influence of various types of geometrical imperfections as well as several residual stress patterns conduct to the next recommendations.

A specific sub-study providing a comparison between experimental tests and numerical results proved the reliability and consistency of the sets of imperfections studied throughout the parametric studies. The following observations concern the method and parameters to use, to account for initial geometrical imperfections:

- even though it constitutes a reliable method, the use of the 1<sup>st</sup> buckling mode shape presents a lack of adaptability and the introduction of an initial deformed shape by means of sinusoidal functions was preferred;
- sections of intermediate slenderness highlighted the most important discrepancy between the various sets of imperfections considered;
- numerical simulations including an imperfection pattern characterised by an amplitude  $a/400$  applied per plate reached the highest ultimate resistances whereas results with an amplitude  $a/100$  were too conservative;
- an equal imperfection amplitude applied to each plate and corresponding to the average between  $a_w/200$  and  $a_f/200$  led to non-conservative results since it decreases the amplitude applied to the plate governing buckling;
- the use of the dimension ( $a_f$  or  $a_w$ ) of one of the plate composing the section to define the half-wave period did not produce important differences from the results obtained with the average between  $a_f$  and  $a_w$ ;
- half-wave period applied independently per plate procured too favourable results for some cases, and, even though this half-wave period is relevant, this set of imperfections was not adopted.

Thus, the adoption of an imperfection defined by an amplitude applied  $a_i/200$  per plate and a period corresponding to the average between the web and flanges largest dimension ( $a_f$  and  $a_w$ ) appears to be a reasonable and appropriate choice.

Then, with respect to material imperfections, the parabolic pattern with a maximum residual stress of 235 MPa represents the most suitable choice for a hot-rolled section. Since 100% of the geometrical imperfections is elected, although the parabolic pattern is slightly more favourable than the triangular one (less than 1.5% different), results will remain secure. Moreover, even though the use of the actual yield stress leads to lower resistance, since negligible differences were enhanced and no references in literature justify the attainment of the yield stress for hot-rolled sections, it represents the most reasonable option.

On the other hand, according to welded sections, negligible differences were encountered in the results obtained with the constant pattern and trapezoidal pattern. Hence, the constant residual stress pattern is recommended with a maximum residual stress corresponding to the actual yield stress, since, by enhancing the simpler characteristics, it constitutes the most convenient pattern for utilisation.

## **6 Conclusion**

The major issue related to the introduction of imperfections into FE simulation is due to the lack of guidelines in current standards which deter from using Finite Element software and non-linear analyses.

Hence, investigations by means of numerical simulations, related to the influence of imperfections on the local resistance of open section were carried out. Geometrical imperfections were introduced by means of sinusoidal functions and using the 1<sup>st</sup> buckling mode shape. Several amplitudes and number of half-waves were considered. Moreover, to complete the imperfection influence study, several residual stress patterns were investigated, respectively to both welded and hot-rolled manufacturing processes.

Consequently, the recommendations were provided on section 5. With respect to geometrical imperfections, a sinusoidal function was found to be the most suitable solution to implement. Even though the introduction of the 1<sup>st</sup> buckling mode shape obtained with LBA analysis represents a consistent and reliable method, the use of sinusoidal functions was recommended since it provides more adaptability with greater control. The parabolic residual stress pattern and constant residual shape described in section 2 were recommended for numerical simulations of hot-rolled and welded sections respectively.

Nevertheless, the guidelines specified herein concern uniquely the influence of geometrical and material imperfections on the local resistance of open sections. Further investigation is already available on the influence of imperfections on the member resistance of open-sections (Subramanian et White 2016).

## 7 References

- Boissonnade, N., and H. Somja. 2012. "Influence of Imperfections in FEM Modeling of Lateral Torsional Buckling." *Annual Stability Conference, SSRC*. Grapevine, Texas.
- Boissonnade, Nicolas, Marielle Hayeck, Elsy Saloumi, and Joanna Nseir. 2017. "An Overall Interaction Concept for an alternative approach to steel members design." *Journal of Constructional Steel Research*.
- Davids, A.J., and G.J. Hancock. 1986. "Compression test of short welded I-sections." *Journal of Structural Engineering*.
- ECCS - Committee 8 - Stability 1976. 1976. "Manual on Stability of Steel Structures."
- Eurocode. 2007. "Eurocode 3, Calcul des Structures en Acier, Partie 1-5 : Plaques planes."
- Greiner, R., M. Kettler, A. Lechner, B. Freytag, J. Linder, J.P. Jaspart, N. Boissonnade, et al. 2007. *Semi-Comp: Plastic Member Capacity of Semi-Compact Steel Sections - A more Economic Design*. TU Graz.
- Hayeck, Marielle. 2016. "Development of a new design method for steel hollow section members resistance."
- James, M.N. 2010. "Residual Stress Influences in Mechanical Engineering." *18th Congreso Nacional de Ingenieria Mecanica*.
- Kettler, M. 2008. *Elastic-Plastic Cross-Sectional Resistance of Semi-Compact H and Hollow Sections*. TU Graz.
- Li, Yongzhen. 2014. "Extension of the Direct Strength Method to hot-rolled and welded H profile cross-sections."
- Nseir, Joanna, Marielle Hayeck, Elsy Saloumi, and Nicolas Boissonnade. 2016. "Influence of imperfections on the local buckling response of hollow structural shapes." *Annual Stability Conference, SSRC*. Orlando, Florida.
- Subramanian, Lakshmi, and Donald W. White. 2016. "Resolving the disconnects between lateral torsional buckling experimental tests, test simulations and design strength equations." *Journal of Constructional Steel Research*.
- Thiébaud, Raphaël, Jean-Paul Lebet, André Beyer, and Nicolas Boissonnade. 2016. "Lateral Torsional Buckling of Steel Bridge Girders." *Annual Stability Conference, SSRC*. Orlando, Florida.
- Yun, Xiang, Joanna Nseir, Leroy Gardner, and Nicolas Boissonnade. 2016. "Experimental and numerical investigation into the local imperfection sensitivity of hot-rolled steel I-sections." *CIMS, 7th International Conference on Coupled Instabilities in Metal Structures*. Baltimore, Maryland.